

1 Article

2 **Holocene coastal evolution of the eastern Iranian**
3 **Makran: Insights on seismic activity based on beach**
4 **morphology and sedimentology**

5 **Raphaël Normand^{1*}, Guy Simpson¹, Frédéric Herman², Rabiul Haque Biswas² & Abbas Bahroudi³**

6 ¹ Department of Earth Sciences, University of Geneva, Rue des Maraîchers 13, 1205 Geneva, Switzerland.
7 Raphael.normand@unige.ch, guy.simpson@unige.ch

8 ² Institute of Earth Surface Dynamics, Faculty of Geosciences and Environment, University of Lausanne, 1012
9 Lausanne, Switzerland. Frederic.herman@unil.ch, rabiulhaque.biswas@unil.ch

10 ³ Exploration department, School of Mining Engineering, University of Tehran, Northern Kargar avn, P.O.
11 Box 11365-4563, Tehran. Bahroudi@ut.ac.ir

12

13 * Correspondence: raphnormand@gmail.com

14 Academic Editor: name

15 Received: date; Accepted: date; Published: date

16 **Abstract:** The Makran coast displays evidence of surface uplift since at least the Late Pleistocene,
17 but it remains uncertain whether this displacement is accommodated by creep on the subduction
18 interface, or in a series of large earthquakes. Here, we address this problem by looking at the short
19 term (Holocene) history of continental vertical displacements recorded in the geomorphology and
20 sedimentary succession of the Makran beaches. In the region of Chabahar (Southern Iran), we
21 study two bay-beaches through the description, measurement and dating of 13 sedimentary
22 sections with a combination of radiocarbon and Optically Stimulated Luminescence (OSL) dating.
23 Our results show that lagoonal settings dominate the early Holocene. A flooding surface associated
24 with the Holocene maximum transgression is followed by a prograding sequence of tidal and
25 beach deposits. In Pozm bay, we observe a rapid horizontal progradation of the beach ridge
26 succession (3.5 m/y over the last 1950 years). A 3150 year old flooding surface within the
27 sedimentary succession of Chabahar bay is interpreted as a coseismic subsidence event. Although
28 the western Makran subduction zone has been aseismic for several centuries, the coastal geological
29 record reveals the occurrence of a sudden vertical displacement and complex uplift patterns, which
30 in the context of a subduction zone could reasonably be attributed to the occurrence of ancient
31 earthquakes.

32 **Keywords:** Makran, coastal processes, coseismic subsidence, Holocene uplift, headland-bay beach,
33 beach progradation

34

35 1. Introduction

36 The Makran coast, in southeastern Iran, sits above oceanic lithosphere of the Arabian plate that
37 is currently subducting northward under Eurasia. The coast has clearly experienced long-term uplift
38 throughout the Late Pleistocene, as evidenced by the presence of emerged sequences of marine
39 terraces, some of which outcrop at more than a hundred meters above present sea-level [1–3]. In the
40 eastern Makran (Pakistan), surface uplift of the coastal margin appears to be closely linked with
41 large earthquakes, the last of which was a Mw 8.1 thrust event in 1945 [4,5]. However, in the western
42 segment of the Makran (Iran), there is no obvious historical evidence for large earthquakes in the last
43 1000 years [6–9]. It is currently unclear whether the lack of seismicity reflects a different mechanical
44 behavior at the subduction interface, or if infrequent large earthquakes occurred in the past and
45 should be expected to happen again [10–12]. Here, we studied Holocene beach deposits to try to
46 better understand the nature of vertical motions in the Makran over the last 10'000 years.

47 Due to their close relation to mean sea level, beaches are prone to record relative sea-level
48 changes related to coseismic vertical motions, as commonly observed in subduction zones [13,14].
49 Along a coastline experiencing coseismic uplift, a beach staircase profile can develop due to the
50 sudden abandonment of the active ridge during earthquakes [15]. Inversely, in regions experiencing
51 coseismic subsidence, remobilization of the sediments from the destroyed frontal part of the beach
52 into a new active beach ridge situated further seaward has been observed to happen in the few years
53 following earthquakes [16]. On the other hand, if the western Makran is behaving aseismically, the
54 deformation is accommodated on long time scales and there should be no signs of perturbation in
55 the beaches.

56 Although several studies have considered the long-term uplift recorded by the spectacular
57 Pleistocene marine terraces exposed along the Makran coast [5,17–19], relatively little attention has
58 been focused on the shorter-term record. Paleoseismic studies from the Makran coastline have
59 mainly focused on the tsunami risk associated with megathrust earthquakes within the MSZ
60 [20,21,8,22–25]. A few studies have published paleoseismic evidences associated with the Mw 8.1
61 1945 eastern Makran earthquake [26,10], but geological evidences for older events have rarely been
62 described [27]. Studies focusing on the beach ridge succession of Chabahar bay have not considered
63 the potential for coseismic vertical motion [28–30].

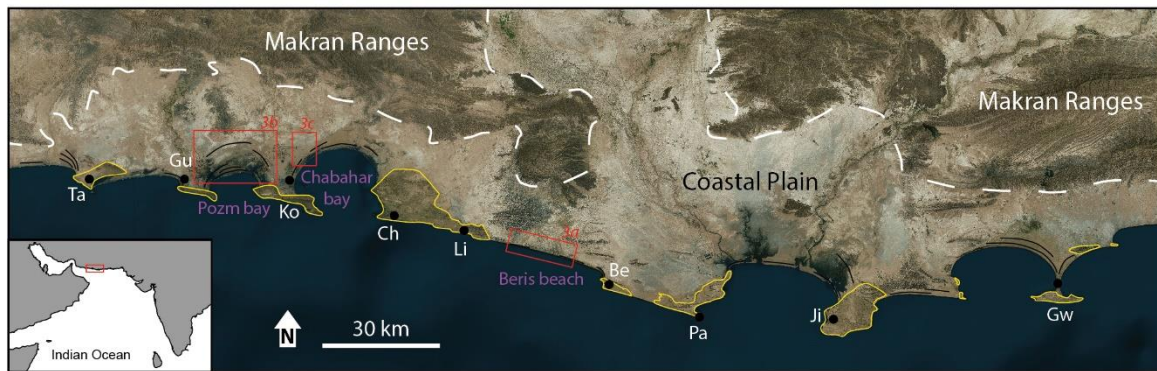
64 In this study, we have analyzed the development of two bay-beaches of the Iranian Makran;
65 Chabahar bay and Beris bay (Fig. 1). We measured 11 and 2 sections respectively in these bays in
66 order to understand the history of the beaches using the sedimentary succession of recent deposits.
67 To add time constrains, we sampled relevant intervals for both radiocarbon and optically stimulated
68 luminescence dating (OSL). Furthermore, we visited and sampled the beach ridge succession of
69 Pozm bay in order to get insights on coastal progradation. Fluvial sedimentary input was assessed
70 through a study of the watersheds of main tributaries. Our results shed light on the landscape evolution
71 of the region over the Holocene, driven by the interaction between sediment input, eustatic sea level
72 variation and vertical tectonic motion.

73 2. Geological setting

74 The Makran subduction zone (MSZ) is the result of northwards subduction of the Arabian plate
75 under Eurasia [4,31,32,10,8]. Although the margin is currently active, as indicated by GPS [33–35]
76 and recently uplifted marine terraces [5,18,36,19,2], seismic activity of the Makran remains relatively
77 low compared to other subduction zones. The eastern segment has experienced several thrust
78 earthquakes, notably the Mw 8.1 in 1945 [4] and a recent Mw 6.3 event in 2017 [12]. However, the
79 western segment (the focus of this study) has seemingly not experienced any thrust earthquake since
80 the historical events of 1008 or 1483 [6,8], whose exact magnitudes, epicenter positions and focal
81 mechanisms remain controversial [9].

82 The bedrock geology at the coastal plain [37,38,5,39–41,2,1,42,43] is dominated by erodible
83 Tertiary marl forming the flat coastal strip (Fig. 1). The coastal plain is occasionally punctuated by

84 prominent headlands, whose bedrock geology is dominated by more resistant, late tertiary
85 calcareous sandstones.



86
87 Figure 1. General satellite view of a segment of the Makran coast (image Bing satellite). White dashed
88 line : rough delineation of the Makran ranges. Black lines : beach ridges. Yellow outlines : protruding
89 headlands. Purple names: studied regions. Red squares: position of Figures 3a, 3b and 3c. Ta : Tang,
90 Gu : Gurdim, Ko : Konarak, Ch : Chabahar, Li : Lipar, Be : Beris, Ji : Jiwani, Gw : Gwadar.

91 The climate in Makran is arid to semi-arid and has been so for at least 5000 years [44–46]. This
92 makes it possible to interpret the Holocene depositional record based on the current coastal setting.
93 The mean annual precipitation is low (127 mm), and occurs mostly during winter [47,48]. Rivers are
94 dry most of the year, but activate during heavy rain episodes resulting in flash flood events
95 inundating the coastal plain and bringing large amounts of sediments to the sea [2,47,1,39,49]. The
96 tide range is micro to mesotidal (1.8-3m) [18,28], and the current wave regime in Chabahar is mostly
97 towards the NNW, with a maximum significant wave height of 3 m [50,28]. Based on a record
98 spanning 1985-2007, winds come mostly from the south and the west [50,51].

99 Only a few previous studies have focused on the Holocene coastal depositional record of the
100 Makran. Radiocarbon dating indicate that they have been developing since the mid-Holocene
101 highstand, around 6000 BP [47,29,30,2,10,48,5,28,52] (supplementary table S1.1). Some authors have
102 argued on the strong mobility of the coastal region during the Holocene, as the coastline seem to
103 have advanced by up to 20 km since the mid-Holocene maximum transgression [47,53]. Moreover, it
104 has been proposed that the Gurdim and Konarak headlands used to be islands that were
105 progressively attached to the mainland by widening tombolos, evolving into the current omega
106 shaped bay morphology (Fig. 1) [2,18,49,29]. The Chabahar bay-beach has been shown to prograde
107 at about 0.7 m/yr between 5438 and 1200 BP, reducing to 0.12 m/yr since then [29]. However, dating
108 results from a recent study of the same strandplain imply a much more continuous progradation of
109 1-2.2 m/yr (faster for younger samples) [28].

110 Signs of the presence of lagoonal systems during the mid-Holocene highstand in the coastal
111 Pakistani Makran has been observed [47,53]. Some of these ancient lagoons have evolved to
112 low-lying flats, such as those observable west of Pasni and northwest of Gwadar, due to their
113 complete filling by fine alluvial sediments. In fact, we can currently observe that the large active
114 lagoons of the Makran, such as that of Kalat or Miani (Pakistan), host river deltas and will one day be
115 entirely filled.

116 3. Methods

117 3.1 Fieldwork

118 Our approach to study the past and present history of the Makran Holocene beaches was to
119 search for natural transects, where beach sedimentary successions could be observed. We visited,
120 logged and sampled two localities. The first transect, where we measured two logs (facies 1 to 6, logs
121 B1 and B2), is a 400m long natural river cut through the longshore beach between Beris village and
122 Lipar lake (hereafter referred to as “Beris beach”) (Fig. 1). The second transect, where we measured

123 eleven logs (facies A to G, logs K1 to K11), is a 4.5 km long man-made trench through the coastal
124 plain near Konarak airport, within Chabahar bay (Fig. 1). We studied the successions by describing
125 the different facies encountered and their spatial (lateral) and chronological (vertical) relation with
126 each other. Ultimately, we try to interpret these facies in terms of depositional setting, with the help
127 of observations made on the current Makran coastal depositional system, in order to have an idea of
128 the Holocene history of these beaches relative to the Holocene sea-level evolution. Additionally, we
129 visited the strandplain within Pozm bay, between Pozm and Gurdim villages (Fig. 1), where we
130 sampled and dated beach ridges at several intervals in order to understand the amount of beach
131 progradation in the bay. We also measured a topographic profile through the beach ridge succession
132 with a hand-held GPS (vertical error: 20% of the measure (source: Garmin)) (supplementary table
133 S1.2-3). Additional field pictures can be found in the data repository [54].

134 3.2 Dating

135 At Pozm bay, we sampled shells from within the abandoned beach ridges. We also sampled a
136 beach ridge deposit situated as close as possible to the Holocene paleoclipf for OSL dating. At Beris
137 beach, we sampled the oldest (most northern) part of the beach for both radiocarbon and OSL, in
138 order to get an idea on the timing of the start of beach deposition. The OSL sample was taken
139 directly at the foot of the Holocene paleoclipf, carved within Tertiary marls.

140 Within the sedimentary logs, we sampled for both radiocarbon and OSL where we observed
141 significant changes in facies in order to put timings on the events responsible for the changes.
142 RN16-29 was sampled in life position, however other samples could not be sampled in life position,
143 due to the nature of the facies in which they were sampled. Therefore, an overestimation of the real
144 age of the deposit due to shell sample reworking is possible.

145 3.2.1 Radiocarbon dating

146 Aragonite shell samples were collected from the deposits for radiocarbon dating. We studied
147 the samples in the lab with SEM secondary electron images and analyzed them with X-ray
148 diffraction (XRD) in order to estimate their state of recrystallization. From the XRD spectra of the
149 sample, we were able to determine if the aragonitic shell had been partially recrystallized to calcite.
150 We added graphite as complementary material into the sample holder when not enough shell
151 material was available (graphite peaks do not interfere with those of calcite or aragonite). A few
152 samples (tagged RN15-...) were sent to Beta Analytics Inc. where they were prepared, bleached and
153 analyzed with the traditional AMS counting method. The other samples (tagged RN16-...) were sent
154 to the laboratory of ion beam physics, at the Eidgenössische Technische Hochschule Zürich (ETHZ),
155 where they were treated and analyzed following the methods described by Hajdas [55].
156 Conventional ages were calibrated with Oxcal 4.2 [56] with the calibration curves IntCal 13 and
157 Marine 13 [57], and a δ_{R} value of 236 ± 31 years, as calculated using the website
158 <http://calib.org/marine/> based on local values [58,59]. Results are presented in Table 1. Additional
159 measurements information, XRD results and SEM images of shells can be found in [54].

160 3.2.2 OSL dating

161 For OSL dating, we targeted sandy facies, poor in shell fragments and pebbles. Foreshore and
162 shoreface facies are described as good dating target for OSL, because complete bleaching prior to
163 burial is likely [60,61]. Samples were taken by hammering a stainless steel tube into the sediment
164 (tube dimensions: 4 cm diameter, 20cm length). In the lab, we removed the material that had been in
165 contact with the light (~4 cm), and analyzed the unexposed internal part of the tube. We treated the
166 samples with the usual preparation methods to isolate 90-150 μm quartz grains through sequential
167 treatment with HCl, H₂O₂, sodium polytungstate density separation, Frantz magnetic separation and
168 HF treatment.

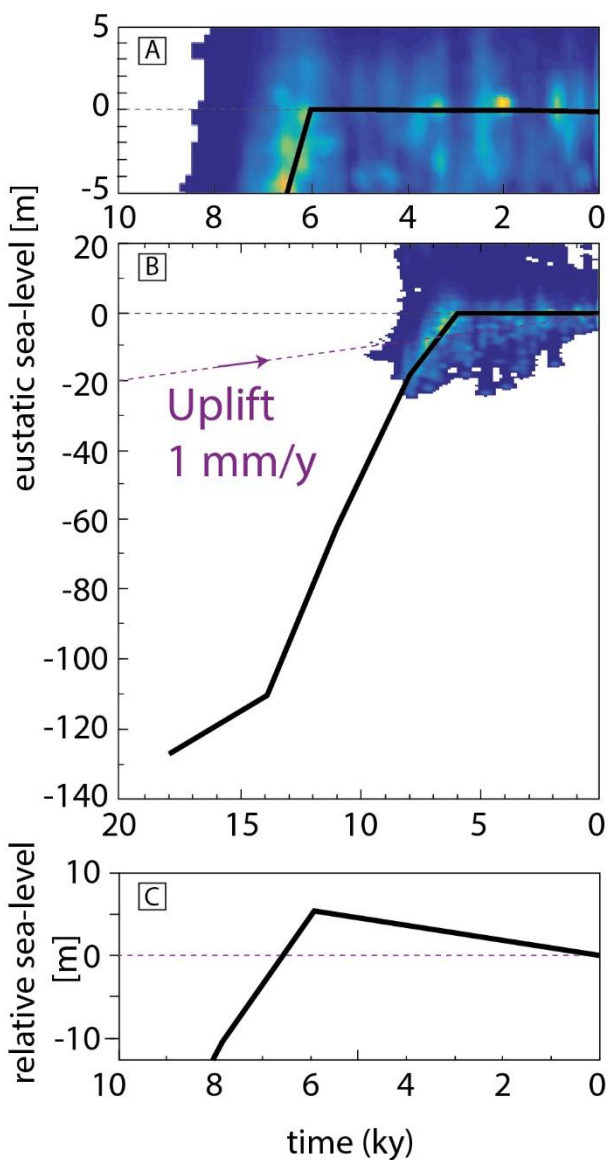
169 The burial dose or equivalent dose (D_e) was determined by measuring the luminescence signals
170 on 24 aliquots per sample (each aliquot contains ~100 grain) using the SAR protocol of Murray and

171 Wintle [62]. We used the Risø TL/OSL-DA-20 reader at the Institute of Earth Surface Dynamics
 172 (University of Lausanne). Results were processed with the Analyst 4.31.7 software [63]. Each aliquot
 173 was evaluated according to the following acceptance criteria: recycling ratios at 10%, maximum test
 174 dose error at 10%, maximum recuperation at 10% of the natural signal and maximum paleodose
 175 error at 20%. Only 1 out of the 120 analyzed aliquots ended up being rejected. D_e values were
 176 assessed with the central age model [64]. The radioactive elements (U, Th, K and Rb), measured
 177 using ICPMS (from ActLabs, Canada), were used in order to calculate the environmental dose with
 178 the DRAC software [65]. The reliability of the protocol and zeroing of clock at the time of deposition
 179 was assessed with a dose-recovery test [66] on 4 representative samples. We exposed the samples to
 180 natural light for 48 continuous hours before measuring the natural signals (to check the residual
 181 dose). Additionally, after artificially bleaching the sample, we measured the recovery of an

artificially given dose of 300 s (~36 Gy) using the same SAR protocol. Dose recovery ratios (recovered dose/ given dose) are 0.8 to 1.01. Results are presented in Table 2. More details on measurements and age calculations are presented in [54].

3.3 Sea-level curve

Knowledge of the sea-level behavior during the Holocene is of utmost importance to study the beaches developing during this period. A number of complex sea-level curves have been published from localities around the Makran [67,68], but they are all different in their details. For our study we have focused on the simple Oman Sea curve proposed by Lambeck [68]. This curve predicts a sea-level rise until 6000 BP, where the sea level stabilized to its current position until today. Additionally, we used the sea-level marker database compiled by Hibbert et al. [69] to build a sea-level probability density plot against which we compared the curve of Lambeck [68]. We screened the database to isolate data from localities close to the Makran (Mauritius, Reunion Island, India, Sri Lanka and the Maldives) and to remove the data without a provided PRSL and error. We built the density plot using a monte carlo simulation with 10000 iterations. The age and depth values for each iteration were generated randomly following a normal distribution (for ages and Z_{cp}) and a coral-species-specific depth distribution provided by the authors. For data not originating from coral species, we used the PRSL values provided by the



214

215 database with a normal distribution. The result of the density plot closely resembles the curve of
 216 Lambeck [68], so we used this curve as an approximation of the sea-level history during the

217

Holocene (Fig. 2). Continental uplift has an impact on the relative sea-level curve and should be taken into consideration. Figure 2c shows the relative sea-level behavior on a coast uplifting at an arbitrary value of 1 mm/yr.

Figure 2. Simplified sea-level curve for the Holocene. (a) Sea-level curve of Lambeck [67] drawn with results of the monte-carlo simulation described in section 3.3. (b) Sea-level-time curve at different scale than shown in A. The purple line represents an uplift of 1 mm/yr. (c) Holocene relative sea-level changes on an uplifting coast (here, hypothetical scenario of 1 mm/yr).

222

223

224 *3.4 Calculation of Holocene uplift rates*

225 To calculate mean uplift rates for small time scales such as the Holocene, we have to know the
 226 altitude relative to mean sea-level at which the sampled material deposited in order to get a precise
 227 estimation of vertical displacement. For this, we use the method presented in Rovere et al. [70]
 228 combined to the general uplift formula of Lajoie [71];

$$U = (E - \text{RWL} - e) / A \quad (1)$$

229 where U is the mean uplift rate, E is the current elevation of the sample, RWL is the mean
 230 altitude relative to mean sea-level at which the sample deposited, e is the eustatic correction (see Fig.
 231 2) and A is the age.

232 Based on the method of Rovere et al. [70], we estimated the upper limit (U_1), lower limit (L_1),
 233 indicative range (IR) and reference water level (RWL) of beach and lagoonal deposits of the Makran,
 234 which we use for uplift rate calculations. For beach deposits, a good sea-level marker is the interface
 235 between intertidal sediments and the eolian sand cap [72,73]. However, because it could not be
 236 identified in the field near the sampled material, we use the estimates proposed by Rovere et al. [70].
 237 Details are provided in supplementary table S1.4.

238 We have adapted the uplift formula to account for the errors on the different terms in order to
 239 get minimum and maximum values of uplift, or uplift ranges [74,19].

$$U_{\min} = [(E - \Delta E) - U_1 - e] / (A + \Delta A) \quad (2)$$

$$U_{\max} = [(E + \Delta E) - L_1 - e] / (A - \Delta A) \quad (3)$$

240 We know the errors on all terms, except that for the eustatic curve, although we recognize that
 241 the eustatic curve can be a significant source of uncertainty.

242 **4. Results**

243 Radiocarbon and OSL dating results are compiled in Table 1 and Table 2, respectively, and
 244 presented in Fig. 3.

245

247 Table 1. Result of radiometric dating. Details in the data repository [54].

Sample	Coordinates [dd.dd°]	Area	Shell type	Radiocarbon age		Comments	Beach progradation rate m/yr
				Conventional ± 1σ BP	Calibrated ± 2σ * Cal BP		
RN15-P3	25.384522°N, 60.233041°E	Pozm bay	Bivalve	590 ± 30	54 ± 54	290m f.c.**	> 0.6
RN15-P7	25.387667°N, 60.232500°E	Pozm bay	Bivalve	490 ± 30	39 ± 39	660m f.c.**	> 3.3
RN15-P15	25.394817°N, 60.230150°E	Pozm bay	Bivalve	810 ± 30	184 ± 116	1450m f.c.**	> 4.8
RN15-P18	25.397750°N, 60.228133°E	Pozm bay	Bivalve	1620 ± 30	931 ± 112	1840m f.c.**	> 0.6
RN15-24	25.429833°N, 60.434300°E	Chabahar Bay	Bivalve	4240 ± 30	4010 ± 135	1500m f.c.**	0.4
RN16-18	25.428866°N, 60.434752°E	Chabahar Bay	Bivalve	6883 ± 22	7167 ± 101		
RN16-19	25.428866°N, 60.434752°E	Chabahar Bay	Gastropod	3465 ± 20	3041 ± 121		
RN16-29	25.458804°N, 60.431895°E	Chabahar Bay	Bivalve	5969 ± 21	6138 ± 117	In life position	
RN16-34	25.439082°N, 60.431512°E	Chabahar Bay	Bivalve	5903 ± 21	6067 ± 113		
RN16-36	25.439082°N, 60.431512°E	Chabahar Bay	Bivalve	6915 ± 22	7218 ± 84		
RN16-37	25.438028°N, 60.431665°E	Chabahar Bay	Bivalve	5602 ± 21	5743 ± 115		
RN15-89	25.196317°N, 61.086100°E	Beris beach	Bivalve	4590 ± 30	4506 ± 131	460m f.c.**	0.1
RN16-11	25.219917°N, 60.984411°E	Beris beach	Gastropod	5744 ± 21	5874 ± 107		
RN16-41	25.220263°N, 60.984910°E	Beris beach	Gastropod	8200 ± 23	8432 ± 88		
RN16-44	25.220263°N, 60.984910°E	Beris beach	Bivalve	8612 ± 23	8940 ± 146		

248

249 *Calibrated using Oxcal 4.2 [56], with the curves IntCal 13 and Marine 13 [57]. Reservoir correction, Delta_R = 236±31 years for Makran, according to the website,
250 <http://calib.org/marine/>

251 **f.c.: From the coastline

252

253
254

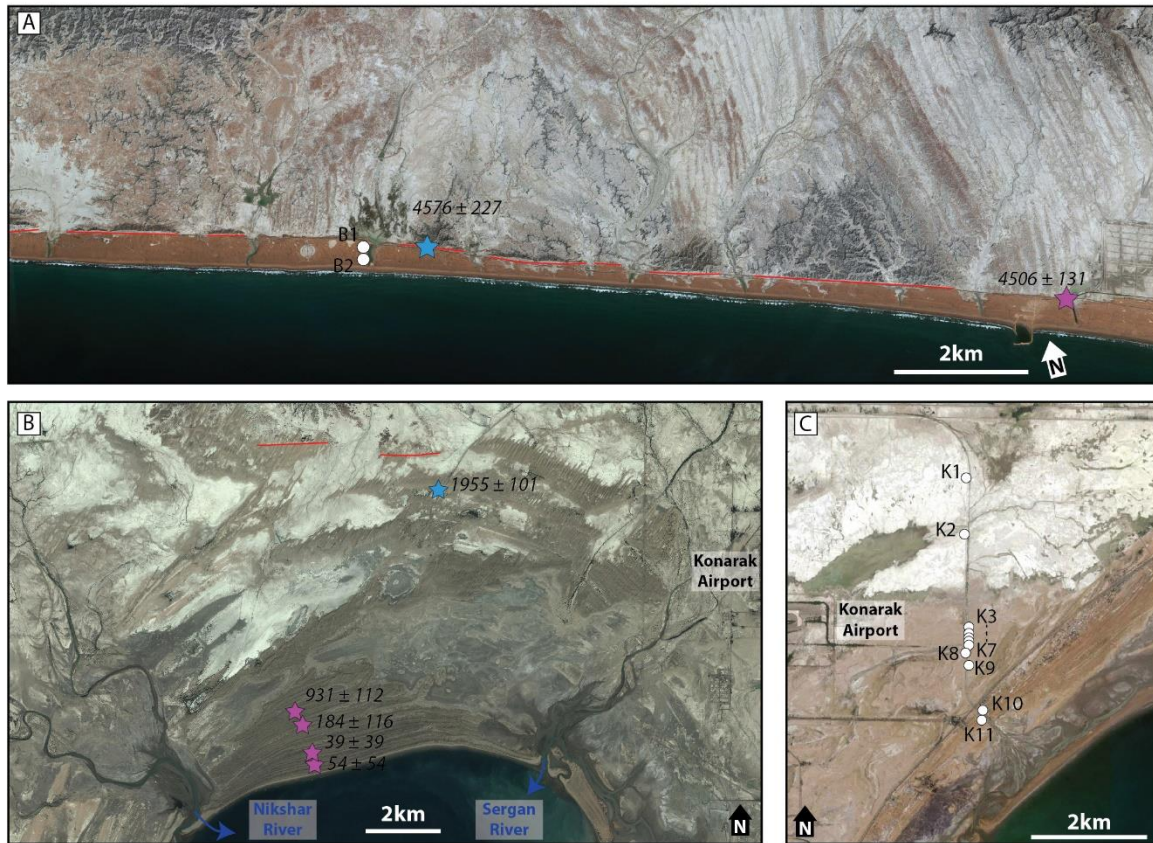
Table 2. Results of OSL dating. Details in the data repository [54].

Area	Comments	Sample	Sample depth [m]	Paleodose CAM ± 1σ [Gy]	N° of Aliquots out of 24	RSD %	OD %	U ppm	Th ppm	K %	Rb ppm	Water content %	Env. dose [Gy / ka]	Age ± 1σ [a]
Pozm Bay	7km from the coastline	RN17-28	0.5 ± 0.1	2.710 ± 0.121	23	22.3	20	1.2 ± 0.05	3 ± 0.11	0.714 ± 0.02	24 ± 1.8	2 ± 2	1.386 ± 0.04	1955 ± 101
Chabahar bay	K3, Above FS	RN17-35	0.5 ± 0.1	4.489 ± 0.206	24	23.6	21	1.4 ± 0.06	3.7 ± 0.14	0.672 ± 0.02	24 ± 1.8	2 ± 2	1.438 ± 0.04	3123 ± 163
Chabahar bay	K6, Below FS	RN17-36	0.7 ± 0.2	4.368 ± 0.230	24	21.0	25	1.2 ± 0.05	3.7 ± 0.14	0.664 ± 0.02	25 ± 1.9	2 ± 2	1.371 ± 0.03	3187 ± 186
Chabahar bay	K11	RN17-37	2 ± 0.5	2.287 ± 0.073	24	17.2	15	2.3 ± 0.1	2.9 ± 0.11	0.498 ± 0.01	16 ± 1.2	2 ± 2	1.369 ± 0.03	1670 ± 67
Beris beach	At the base of the cliff	RN17-44	0.3 ± 0.1	5.929 ± 0.242	24	23.1	19	3.1 ± 0.13	2 ± 0.07	0.241 ± 0.01	11 ± 0.8	2 ± 2	1.296 ± 0.04	4576 ± 227

255 *4.1 Fluvial sedimentary input*

256 One of the major factors controlling the development and progradation of the coast is the
257 sedimentary budget. We infer that the sedimentary input in the Makran mainly originates from 4
258 sources e.g., [75,45,76,77,73,78]; (1) alongshore transport of sea-floor sediments, (2) erosion of
259 nearby headlands, (3) eolian transport and (4) river input. These sources are all linked to climatic
260 conditions, which remained relatively constant in the Makran since the start of the Holocene.
261 However, we observed the presence of ancient river channels within the low coastal plain (Fig. 4a,
262 4b) indicating that the Makran Rivers might have switched from one bay to another throughout the
263 Holocene, drastically modifying the sedimentary budget locally. We gathered information on river
264 watersheds in order to understand where fluvial sediments input the Oman Sea and how fluvial
265 sedimentary input can influence beach progradation. We used a ASTER DEM (30m), which we
266 analyzed using the Topotoolbox from matlab [79,80]. A presentation of river input into the Oman
267 Sea near the Chabahar region is presented in Fig. 4a.

268 The eastern bay of Jiwani receives a major part of the Makran fluvial input since it hosts the
269 mouths of both the Dasht and Pishin watersheds, with drainage areas respectively of 29000 km² and
270 20600 km² (second and third largest of the Makran). Beris beach receives fluvial input from small
271 watersheds, each less than 80 km². Chabahar bay is currently only fed by two small watersheds, of
272 max. 500 km². Pozm bay, however, is receiving sediments from two major rivers, the Nikshar and
273 Sergan rivers, with watersheds of 5400 and 1115 km², respectively. Ancient river channels suggest
274 that the Nikshar and Sergan rivers might have flown towards Gurdim and Chabahar bays,
275 respectively, at some point during the Holocene. The majority of the sand-sized material brought
276 into the Oman Sea by the rivers comes from erosion of the Makran ranges, northwards of the coastal
277 plain (Fig. 4a brown numbers). In this respect, small watersheds, mostly draining the fine-grained
278 bedrock of the coastal plain, bring little coarse material to build beaches.
279



280
281
282
283
284
285
286
287

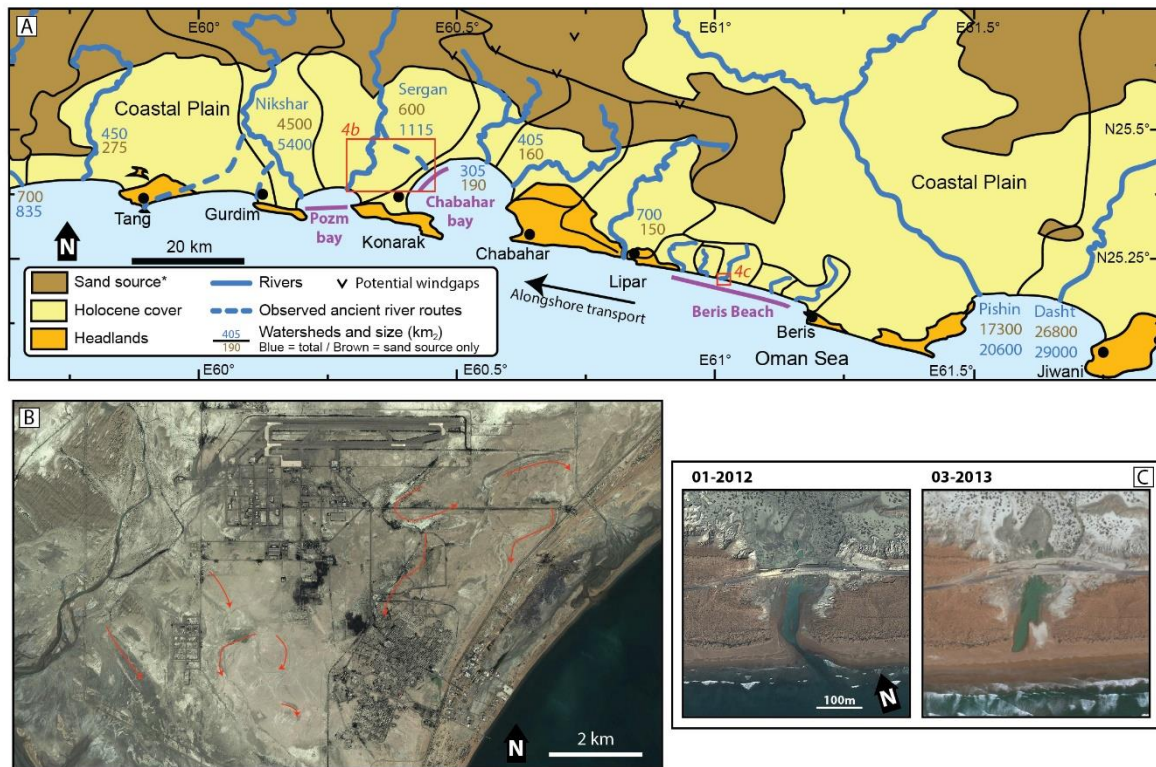
Figure 3. Satellite images of the studied beaches and localization of sampled material and measured logs. Legend: Blue star : OSL sample. Purple star: radiocarbon sample, white circles: stratigraphic logs positions, red lines: paleocliff of the mid-Holocene maximum transgression. (a) Beris beach, localization of the stratigraphic logs B1 and B2 and the dated samples (this study). Image from Google Earth (b) Pozm bay, localization of the dated samples. Image from Bing satellite. (c) Chabahar bay, localization of the stratigraphic logs K1-K11, along a man-made trench near Konarak airport. Image from Google Earth.

288 *4.2 Beach geomorphology*

289 Along the Makran coast, the important contrast in rock resistance between the two main
290 outcropping lithologies (sandstones and marls) has promoted the development of headlands and
291 bay-beaches, e.g., [77,81,78]. Wave action erodes faster through soft marl bedrock than through
292 indurated sandstones, which causes the coastline to develop into deep bays and protruding
293 headlands. Material eroded from headlands, exposed to wave attack, is transported by alongshore
294 currents and preferentially redeposited in embayments, together with continental fluvial input, to
295 form prograding beaches [78,77].

296 The presence of headland and bays favors the formation of a concave beach morphology in the
297 shadow zones behind headlands (Fig. 1). These crenulated beaches best develop when waves
298 approach the coastline with a steep angle of incidence and are facing towards the main alongshore
299 current direction [82,83]. Most bay-beaches of the western Makran are crenulated, facing towards
300 the west, implying a dominant wave direction towards the NW throughout the Late Holocene, as
301 recently measured in Chabahar by [50] (Fig. 1, west of Pasabander). Consequently, from this
302 dominant wave direction, alongshore currents are expected to flow from east to west [75].
303 Interestingly, the crenulated bays of the eastern Makran (Pakistan; Fig. 1 east of Jiwani) face in the
304 opposite direction, suggesting a mirrored wave and alongshore regime.

305



306

307

308

309

310

311

312

313

314

315

Figure 4. Fluvial input in the Chabahar region. (a) Map of Chabahar region with the watersheds contours. Total watershed size is expressed in blue, whereas the watershed area of hard tertiary bedrock (sand source for beaches) is expressed in brown. Purple = studied regions. *Outcropping rocks estimated to be the source of sand-sized material delivered in the Oman Sea by rivers. (b) Google Earth satellite image near Konarak airport. Ancient river paths are visible in the landscape (some outlined with red arrows), implying that the Sergan river used to flow into Chabahar bay. (c) The succession of satellite images shows that the evolution of the beach at the river mouth is influenced by floods. The river bursts through the beach ridge during floods and is re-built by the waves between flood events. N25.209° E61.022°. Images from Google Earth.

316 4.2.1 Beris beach

317

318

319

320

321

322

323

324

325

326

327

328

329

330

331

332

333

Beris beach is 30km long and is built on Tertiary marl bedrock between two rocky headlands (Fig. 1, Fig. 3a). Since re-occupation of the coastline by the sea in the Early Holocene, rapid wave erosion of the bedrock marls has taken place, forming a bay bordered by more resistant headlands [77,78]. The high marl cliffs that punctuate the back of this beach stand as relicts of the maximum extend of coastal regression that peaked shortly before ~4500 BP, according to our dating results (see below). Since then, relative sea-level fall has favored beach progradation. Its characteristic seaward-concave plan shape (eastern end) is the result of beach building by wave refraction around Beris headland under a NW predominant wave direction [83,82].

At Beris beach, the oldest beach ridge was sampled at two different locations and dated with two different methods that both yielded an age of ~4500 BP indicating the start of beach build up at that time. The OSL sample (RN17-44) was sampled at the base of the paleoclipf, such that it should correctly estimate the start of beach deposition. Previous dating results from this beach include ages at 3976 ± 29 and 3646 ± 17 BP [48] and 7605 ± 75 BP [10]. The latter, significantly older than other results, is from dating of a lithofaga mollusk found within a boulder that might have been reworked during the transgression. The top sample of B1, dated at 5744 ± 21 BP also postdates the supposed age of the first beach ridge but still indicates, together with the other results cited, that Beris beach was deposited and has prograded after the mid-Holocene highstand.

334 The beach receives minor fluvial sedimentary input (Fig. 4a) and as a result, has remained
335 narrow (250-600m wide, Fig. 3a) and has prograded slowly (< 0.1 m/yr) since the mid-Holocene
336 highstand. Other sedimentary sources could be alongshore transport (two large watersheds flow
337 into the nearby Jiwani bay) and erosion of the bordering Beris and Lipar headlands, but the
338 distinctive dark orange color of this beach indicates that most of the sand seems to originate from the
339 orange-colored rocks that outcrop northwards of the beach (Fig. 3a). The western part of the beach is
340 nearly linear and is intermittently cross cut by river channels hosting lagoons (Fig. 3a, Fig. 4c).
341 Looking over a succession of satellite images covering several years, we can see that the river incises
342 through the beach during flash floods, whereas wave action re-builds a continuous beach ridge
343 shortly after the flood events (Fig. 4c).

344

345 4.2.2 Chabahar bay

346 Chabahar bay is a 20km wide and 17 km deep omega-shaped bay situated between the two
347 prominent headlands of Chabahar and Konarak (Fig. 1). The onshore central part of the bay is
348 occupied by an up to 5 km wide plain of prograding beach ridges flanked by two lagoonal systems
349 on its eastern and western sides. Similar to Beris beach, the bay-headland configuration appears to
350 be due to contrasting rock strengths between the bay (marl) and headland (sandstone). The omega
351 shape of the bay is due to wave diffraction around the two headlands, similar to what can be
352 observed, in a smaller scale, behind human made breakwaters originally separated from the
353 coastline [84]. Hence, it is possible that the rocky headlands of Konarak and Gurdim were detached
354 from the main land at the start of the Holocene as has been proposed by others [2,18,49,29].

355 Although the presence of this wide strandplain hints towards a high input of sediment, Chabahar
356 bay currently receives sediments from only two small watersheds draining mainly the fined-grained
357 rocks of the coastal plain (Fig. 4a). Part of the sand sedimentary input comes from the erosion of the
358 nearby headlands (mainly Chabahar headland, due to its size, upstream position and sandstone
359 dominated bedrock). The ancient river channels observable around Konarak airport (Fig. 4b) suggest
360 that the Sergan River used to flow into the Chabahar bay, nearly tripling the fluvial coarse-grained
361 input. Results from Gharibreza [29] indicate that beach progradation in Chabahar bay substantially
362 slowed down at 1200 BP, which might be the moment when the Sergan river diverted towards Pozm
363 bay. However, recent results of Shah-Hosseini et al. [28] suggest an opposite scenario, where beach
364 progradation increases until today. We also observed potential wind gaps in the Makran Ranges
365 north of Chabahar, hinting towards ancient river routes towards the Chabahar bay (Fig. 4a).
366 However, these routes were probably diverted due to rock uplift, on timescales greater than the
367 Holocene.

368 4.2.3 Pozm Bay

369 Pozm bay is another omega-shaped bay delimited in the east by Konarak and in the west by
370 Gurdim headlands. The size of the bay (12 km wide, 6.5 km deep) is considerably smaller than that
371 of the neighboring Chabahar bay. However, the paleocliff, that we observed within the Tertiary marl
372 bedrock, is 9.4 km away from the current coastline (red line, Fig. 3c), implying an important coastal
373 progradation. The oldest ridges, situated further from the sea, are partially degraded to elongated
374 and NNE directed eolian dunes, as expected from the two main wind directions, coming from the
375 west and south [50]. The lowlands between the oldest ridges, possibly ancient intertidal lagoons, are
376 transformed into ponds shortly after flash flood events, where fine-grained alluvial deposits decant.
377 Finally, the outer 4 km of the bay hosts a succession of beach ridges, flanked by two active lagoonal
378 systems at the mouths of the Nikshar and Sergan rivers (Fig. 3b, Fig. 4a).

379 We have dated four shell samples from the beach ridges at Pozm bay (from the sea, beach ridge
380 N°3, 7, 15 and 18) (Fig. 3b) to better understand the prograding history of the strandplain.
381 Unfortunately, the two first samples yielded very young conventional ages that could not be

382 accurately calibrated. Nonetheless, we know they should be recent, (a maximum of several hundred
 383 years). The 15th and 18th beach ridges yielded calibrated ages of 184 ± 116 BP and 931 ± 112 BP
 384 respectively. We also sampled one of the oldest beach ridges, close to the observed paleocliff, which
 385 yielded an unexpectedly young OSL age of 1955 ± 101 years. We aimed to sample beach facies, but
 386 we do not exclude the possibility that we might have sampled an eolian deposit ([54], image A_1),
 387 which would yield a younger OSL age (minimum age).

388 Our dating results from the beach ridge succession at Pozm bay indicate three main facts. 1)
 389 According to the OSL results (RN17-28), the active beach ridge was still close to the paleocliff 1955
 390 years ago (i.e. late after the mid-Holocene highstand) (Fig. 3b, blue star). 2) The recent progradation
 391 has been very fast, with a mean value of 5.2 m/yr between 1955 ± 101 years and 918 ± 112 years, and a
 392 minimum of 4.8 m/yr during the last 300 years. 3) Progradation rates seem to have slowed
 393 significantly between 931 ± 112 and 184 ± 116 years ago (Beach ridges P18 and P15) (400 meters in
 394 747 years, or 0.55 m/yr). Nevertheless, a mean progradation rate of 5.2 m/yr over a long period of
 395 1955 years is very high and indicates that this OSL age must be considered with caution (see above).
 396 The rapid recent (<300 years) beach progradation is probably due to a local increase in fluvial
 397 sedimentary input due to the redirection of one (or both) rivers towards Pozm bay (Fig. 4a, 4b).
 398

399 *4.3 Beach sedimentology*

400 The facies description and interpretation of the depositional setting is reported in
 401 supplementary table S1.5. Sedimentary logs, legends and field pictures are compiled in Fig. 5 and
 402 Fig. 7. Additional field pictures can be found in [54], as referred to in supplementary table S1.5.
 403 Sedimentary facies at Beris beach are greatly influenced by fluvial input, as coarse conglomerate
 404 deposits constitute a substantial proportion of the sedimentary succession. In Chabahar bay, the
 405 sedimentation is dominated by lagoonal, tidal and beach deposits. Because the Makran climate has
 406 remained roughly the same for at least the last 5000 years [45,44,46], we base our facies
 407 interpretations on observation of the modern system (Fig. 6, Fig. 8) ([54], images D).

408 The samples from within the sedimentary successions (B1,B2 and K1 to K11) yielded complex
 409 dating results. OSL and radiocarbon results do not always agree with each other and reworking of
 410 some sampled material seems to have taken place. At the northernmost section within Chabahar bay
 411 (K1), a shell sampled in life position within the lower facies, situated directly above the bedrock can
 412 be considered as reliable. It was dated at 6138 ± 117 BP, which corresponds to the timing of the
 413 maximum transgression of the mid-Holocene highstand (Fig. 2).

414 Table 3. Short description and interpretation of the facies of Beris and Chabahar bay cross sections.
 415 More details may be found in supplementary table S1.5.

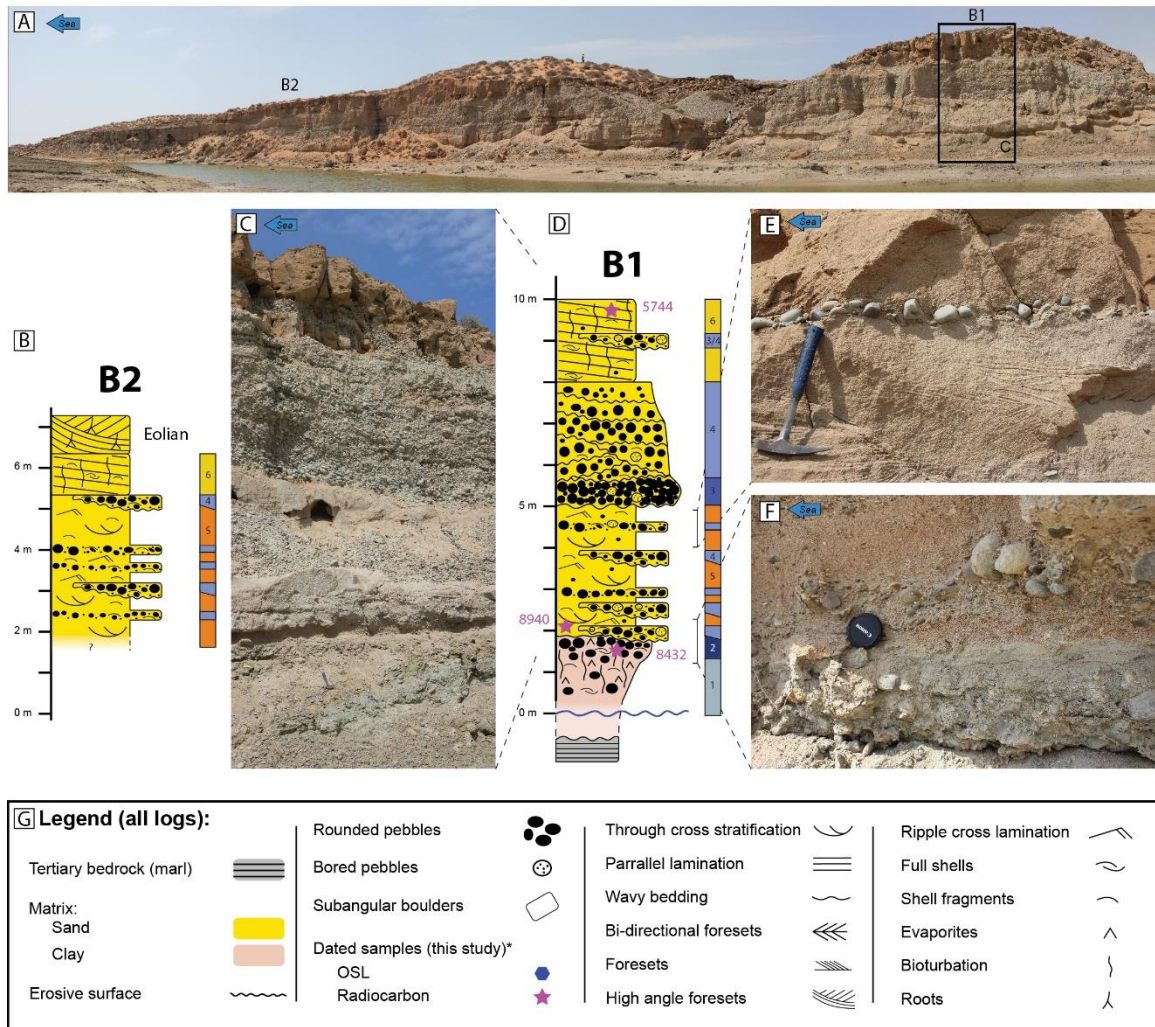
Facies	Short description	Depositional Environment
Beris		
1	Matrix supported, fine-grained laminated deposit	Lagoon
2	Conglomerate, clay matrix	Lagoon with fluvial input
3	Conglomerate, no matrix	Fluvial channel
4	Conglomerate, sandy matrix	Mouth bar
5	Well-sorted sandstone. Cross stratifications	Shoreface

6	Horizontally laminated well sorted sandstone	Beach
Chabahar bay		
A	Laminated fine-grained deposit, evaporites	Supratidal flats
B	Heavily bioturbated fine-grained deposit	Intertidal ponds
C	Sandy deposits, wavy beddings	Intertidal lagoon
D	Erosive base, channelised, bi-directional cross bedding	Tidal channel
E	Same as D, with occasional <20 cm thick mud drapes	Tidal channel
F	Same as D without the channelised morphology	Intertidal / subtidal
G	Horizontally laminated well sorted sandstone	Beach

416

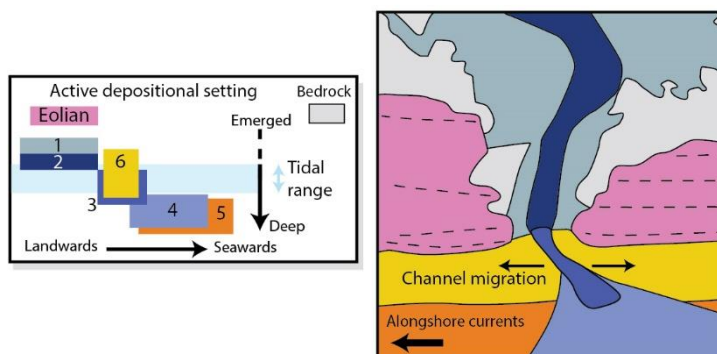
417 4.3.1 Beris beach

418 B1 and B2 represent, respectively, the proximal and distal parts of the system, which can be
419 inferred by their geographical position as well as by looking at their pebble content. The lower part
420 of the sequence indicates the presence of a lagoon at 8432 ± 88 BP occasionally disturbed by flash
421 flood events. After an erosive surface, the sedimentary succession switches to a facies with a major
422 marine influence (richer in sand). Relative sea-level rise at that time (Fig. 2c) explains the presence of
423 this flooding surface (FS). However, we suspect the sample from the sandy layer, dated at 8940 ± 146
424 BP (i.e., older than the underlying sample, see Fig. 5d) to be reworked. Following this event, the
425 system progrades to a more proximal setting as relative sea-level starts to fall following the
426 mid-Holocene highstand and the space created by relative sea-level rise gets filled with sediments.
427 These sediments consist of thick conglomerates with few sand (facies 3), indicating a position within
428 the main channel where erosion of the wave-built sandy layers occurs during successive floods (Fig.
429 4c, Fig. 6). The amount of pebbles decreases upwards and the proportion of sandy matrix increases
430 as the channel migrates away through time. In the distal part of the system (B2), the environment
431 remains marine (dominated by shoreface facies) though occasional thin conglomerate layers suggest
432 sporadic fluvial input associated to the more proximal facies seen in B1. Finally, the upper beach
433 facies in B1 marks the emergence of the succession after the mid-Holocene highstand, though once
434 again, the system continued to be influenced by occasional floods. Since then, the beach has
435 prograded to its current position as the coast uplifted and the relative sea-level fell (Fig. 2c),
436 permitting the incision of the outcrop.



437
438
439
440
441
442

Figure 5. Beris beach stratigraphic logs. (a) Beris beach transect. N 25.219, E 60.985. (b) Log B2. (c) close up of the transect at the position of log B1 (black square in Fig. 5a). (d) Log B1. (e) Close up of facies 5. (f) Close up of the bottom of log B1, the transition from facies 2 to 4-5. (g) Legend for all logs (Figures 5 and 7). *Ages standard deviations are not reported on the figures but can be seen in Tables 1 and 2. More pictures can be seen in the data repository [54], images C.



443
444
445

Figure 6. Beris beach, interpretation of the described facies depositional environment (based on Figure 4c). Black dashed lines: beach ridges.

446 4.3.2 Chabahar bay

447 In the proximal position of the section, the contact between the marl Tertiary bedrock and the
448 first layers of Holocene fine-grained lagoonal deposits was observed ~5 km from the current
449 coastline (K1). This lagoonal layer is dated at 6138 ± 117 BP on a shell in life position; hence, it was
450 deposited during the mid-Holocene highstand. The lagoonal sediments are overlain by a thick (up to
451 3m observed above the surface) layer of intertidal lagoonal muds, outcropping over a lateral
452 distance exceeding 2.5 km (K2). These deposits become progressively sandier towards the sea and
453 about 3 km from the current coastline they are dominated by sands (K4-K8), occasionally cross cut
454 by sandy intertidal channels rich in shell fragments (K5-K8). The layers of intertidal sediments
455 observed in the lower part of logs K3-9 were probably deposited within the same ancient lagoonal
456 system. Those intertidal facies are overlain by layered muds of facies A, interpreted as supratidal
457 deposits (K3-K6, K8-9). This succession is a normal prograding sequence, as could be expected on an
458 uplifting coast (Fig. 2c); the tidal channels are abandoned as the coastline progrades or the lagoon
459 migrates laterally and the intertidal areas become supratidal flats (Fig. 8b).

460 A drastic change in facies is observed in the central portion of the sedimentary logs (K3-K9) as
461 the supratidal layered muds of facies A abruptly transitions to the lower intertidal facies D or F
462 (outlined blue arrows in Fig. 7, see also inset Fig. 8b). This succession is visible in most logs (K3-K9)
463 (Fig. 7). This sedimentary succession implies the creation of accommodation following the
464 deposition of facies A. At K9, a beach facies G overlays the supratidal facies A. Facies G is expected
465 to form at the coastline, whereas A is deposited in a more proximal position (Fig. 8b inset), implying
466 coastal retreat between the depositions of the two layers. Therefore, a relative sea-level rise, or
467 flooding surface (FS), seems to occur within the sedimentary successions, whereas the relative
468 sea-level curve of the Holocene on an uplifting coast would rather be expected to be globally falling
469 (Fig. 2c).

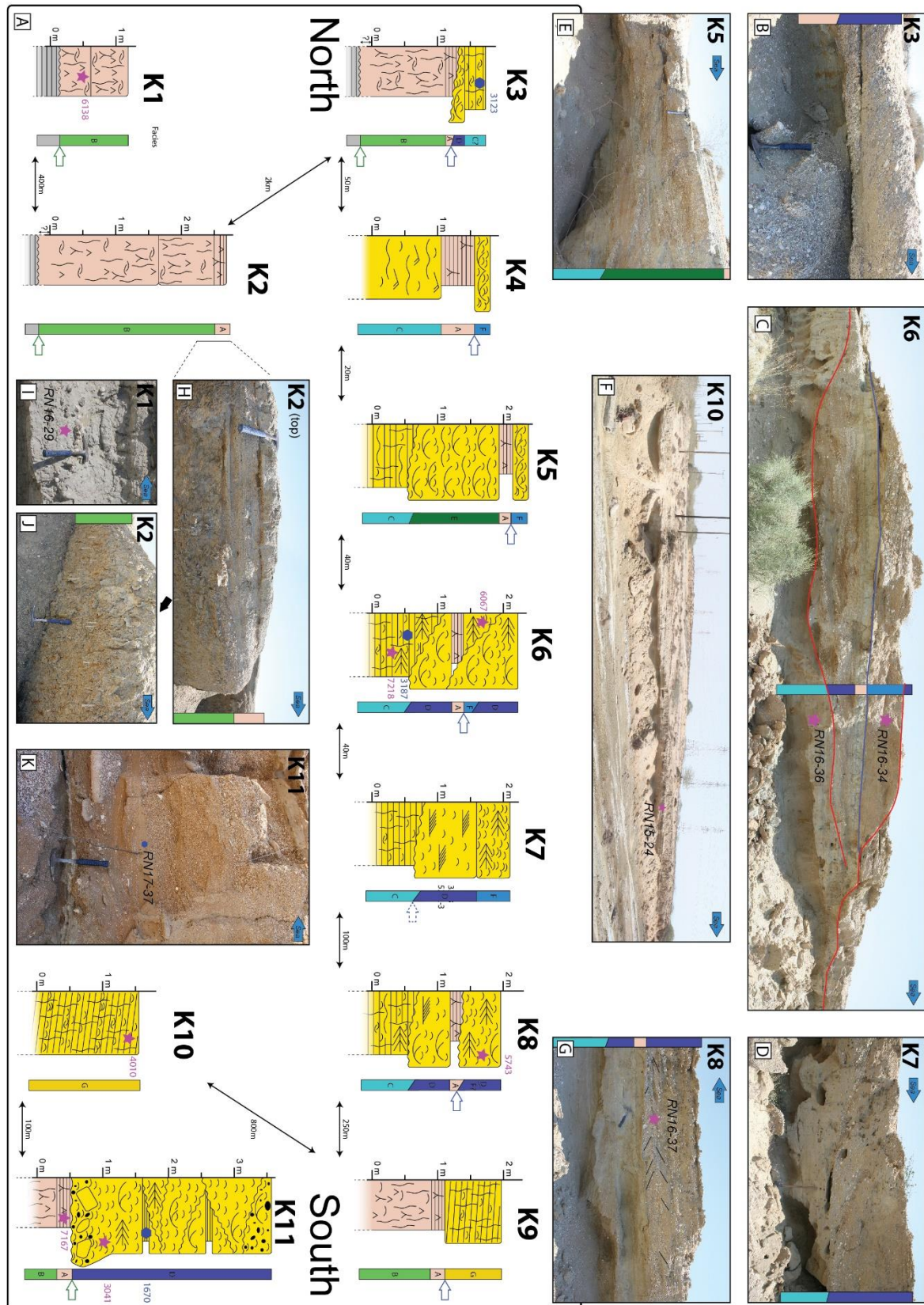
470 We attempted to date the episode of relative sea-level rise observed within the sedimentary logs
471 K3-K9 (FS) (outlined blue arrows in Fig. 7) in order to understand if this was a slow or fast event, or
472 if it might coincide with the mid-Holocene maximum transgression. Unfortunately, the results are
473 unclear, especially because OSL and radiocarbon results do not agree with each other. Therefore, we
474 propose two different interpretations based on either method, since combining both leads to
475 ambiguous conclusions.

476 Based on the radiocarbon age results, the lower layer of lagoonal deposits date shortly before
477 the mid-Holocene highstand (~7000-6000 BP). At that time, the relative sea level was rising (Fig. 2)
478 which seems at odds with the prograding sequence of sediments below the FS (Fig. 7a). Eventually,
479 the sequence becomes emerged, leading to coastal regression, which is expressed in the logs by the
480 flooding surface (FS). After the maximum transgression ~6000 years ago, the relative sea level falls,
481 and the system progrades. Hence, the FS is associated with Early Holocene sea-level rise.

482 Based on OSL dating, the system postdates the mid-Holocene highstand. Samples below and
483 above the FS date at the same age within errors of ~3150 years ago. Therefore, the prograding
484 lagoonal system has been flooded very quickly around 3150 years ago. This rapid relative sea-level
485 rise is at odds with the seemingly steady and undisturbed nature of the sea-level curve at that time
486 (Fig. 2).

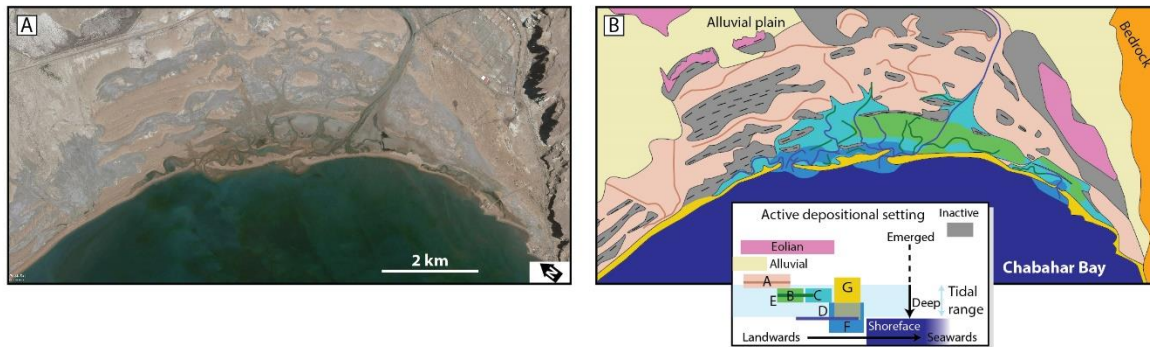
487 The seawards part of the succession is less interesting. Beach deposits, showing the
488 characteristic low angle lamination of the swash zone, can be seen on the northern flank of the
489 channel (K10). On the southern flank, the lower part of the K11 log is made of the supratidal muds of
490 facies A, overlain by an erosive surface and the deposition of sandy facies rich in shells interpreted as
491 facies D. This FS can be associated to the mid-Holocene transgression based on our dating results
492 (Fig. 7a). The presence of decimetric subangular boulders directly above the erosive surface is
493 attributed to ravinement.

494



495
 496
 497
 498
 499
 500

Figure 7. Stratigraphic logs of Konarak Airport section (K1-K11). Vertical scale is not absolute altitude, but height above the bottom of the channel. Blue outlined arrow: Flooding surface (see section 4.4.2). Green arrow : Mid-Holocene transgression. More field pictures can be found in the data repository [54], images B.



501
 502 Figure 8. Chabahar bay depositional setting. (a) Google Earth satellite image of the eastern part of
 503 Chabahar bay (27/1/2015). N25.42°, E60.59°. (b) Interpretation of the described facies depositional
 504 environment. Black dashed lines: beach ridges. Colored full lines: tidal channels. Eolian degradation
 505 of inactive beach ridges is taking place but is difficult to represent graphically.

506 5. Discussion – Paleoseismic evidences

507 5.1 Signals from beach sedimentology

508 We believe OSL results to be more reliable because they directly date sediment deposition and
 509 are not affected by reworking issues. These results suggest that Chabahar bay may have undergone
 510 an abrupt flooding event 3150 years ago. This event might have been caused by vertical land motion
 511 caused by a great earthquake (Fig. 9e). If this was the case, the flooding surface (FS) should also be
 512 expected within the stratigraphic logs of nearby beaches. Unfortunately, the other sections studied at
 513 Beris beach do not contain sediments as young as this event. We find no clear indications for earlier
 514 vertical coseismic displacements within the Beris beach succession. The flooding surface at the base
 515 of the Beris beach sequence is contemporaneous with the Early Holocene eustatic sea-level rise and
 516 therefore does not constitute an evidence for coseismic subsidence. Moreover, most of the
 517 sedimentary facies composing the Beris section (shoreface facies, Fig. 5) do not have a close relation
 518 to the sea-level position (Fig. 6) and therefore should not be affected by minor relative sea-level
 519 changes.

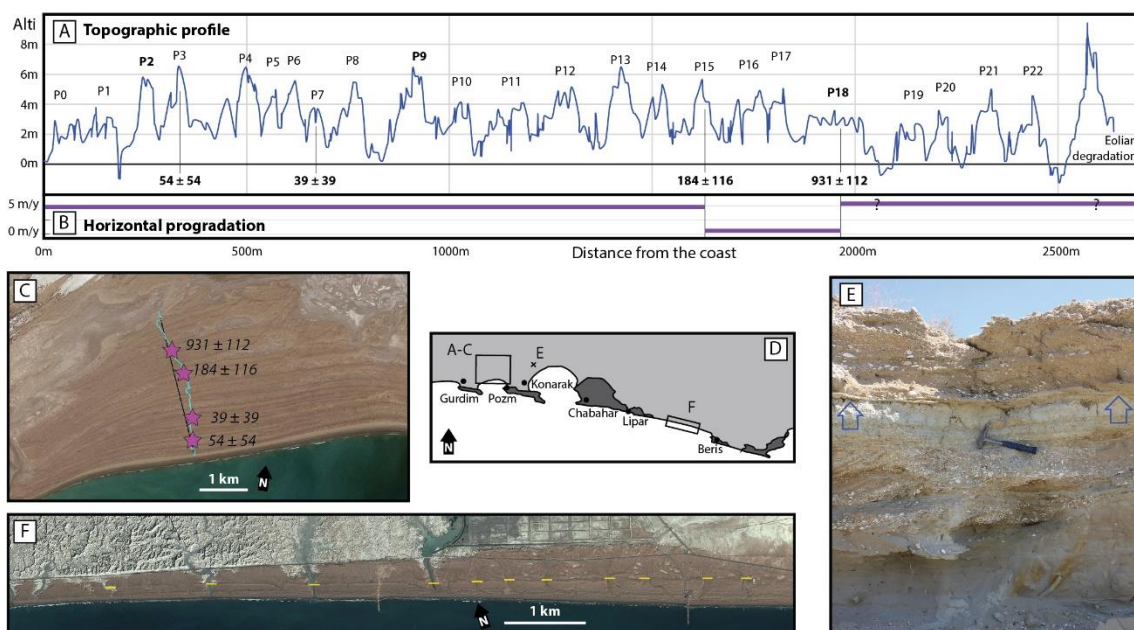
520 From a study of altitudes of dated beach ridges, Shah-Hosseini et al. [28] constructed a relative
 521 sea-level curve of Chabahar bay. Their curve is globally falling over the Holocene, due to an overall
 522 uplifting trend of the land [19]. However, the presence of a plateau (due to a lack of data between
 523 3200 and 2000 BP) could be caused by a subsidence event in 3150 BP, followed by uplift. Large
 524 boulders along the coast of Oman, interpreted as being displaced by tsunami waves originating in
 525 the Makran subduction zone, have been recently dated to 7540 ± 120 cal yr. BP, 1175 ± 115 cal yr. BP
 526 and 265 ± 155 cal yr. BP [85]. The 3150 year old event we describe here could complete this record.

527 In the eastern Makran, Page et al. [5] reported a coseismic uplift of 2m in Ormara during the
 528 1945 Mw 8.1 earthquake, which could seem at odds with the predicted coseismic subsidence that we
 529 propose here for the western Makran. However, the general distribution of thrust coseismic vertical
 530 displacement is well known from both field observations [86–89] and numerical simulations e.g.,
 531 [90,91]. The distance to the trench is an impacting factor controlling the coseismic (and interseismic)
 532 vertical deformation (Fig. 10a, green line). The trench-coast distance is smaller in the eastern than in
 533 the western Makran (~75 km in Ormara, ~130km in Chabahar) favoring coseismic uplift in the east
 534 and coseismic subsidence in the west.

535 5.2 Signals from beach topography

536 We have measured a topographic profile through Pozm bay with a hand-held GPS (Fig. 9a, 9b,
 537 9c, supplementary table S1.2-3). The resulting topographical profile does not indicate a climbing
 538 staircase pattern as might be expected from repeated episodes of coseismic uplift. Rather, the overall
 539 flat profile probably results from normal beach progradation driven by high sediment supply e.g.,

540 [73,72]. However, three beach ridges stand out in their proportions (P2, P9 and P18), and could
 541 potentially be associated to beach sediment rework following coseismic subsidence or a tsunami e.g.,
 542 [16]. P2 is one of the youngest ridges and might be associated with the tsunami of 1945. P9 is recent
 543 ($< 184 \pm 116$ BP), but does not correspond to any known historical earthquake from the western
 544 Makran. P18 (dated at 931 ± 112 BP) could be associated with the tsunamigenic earthquake that
 545 happened in the western Makran in 1008 AD [8]. The slow in beach progradation rates that occurred
 546 between the dated samples at P18 (931 ± 112 y) and P15 (184 ± 116 y) is intriguing. It might be the
 547 effect of a sudden transgressive event before the deposition of P15, followed by resumed
 548 progradation. The topographical profile through Chabahar bay by Gharibreza [29] shows a
 549 prominent beach ridge in a seawards position of their 3481 ± 87 BP sample, which could be
 550 associated with the event 3150 years ago that produced a flooding surface within our studied
 551 sedimentary succession of Chabahar bay (section 4.3.2, Fig. 7a, Fig. 9e). Additionally, at Beris beach,
 552 we noticed a prominent beach ridge halfway between the paleocliff and the sea (yellow dashed line
 553 in Fig. 9f, see also Fig. 1). Unfortunately, this ridge was not dated.
 554



555
 556 Figure 9. Paleoseismic hints in the western Makran beaches. (a) Topographic profile through Pozm
 557 bay-beach ridge succession (see Fig. 9c). No obvious step-like topography can be detected. (b)
 558 Horizontal progradation speed from dated ridges. (c) Satellite view of Pozm bay profile (Fig. 9a).
 559 Image Google Earth at 25.39°N , 60.24°E . The profile is projected on the black line (see supplementary
 560 table S1.3). (d) Geographical situation of the presented pictures. (e) Flooding surface (blue arrows)
 561 within the sedimentary succession of Chabahar bay that might be due to coastal subsidence, dated
 562 ~ 3150 years ago by OSL. $25.439082^{\circ}\text{N}$, $60.431817^{\circ}\text{E}$. (f) Beris beach. A prominent beach ridge,
 563 associated with a topographic step can be observed within the beach (yellow dashed line). Image
 564 Google Earth at 25.18°N , 61.10°E .

565 5.3 Holocene uplift rates

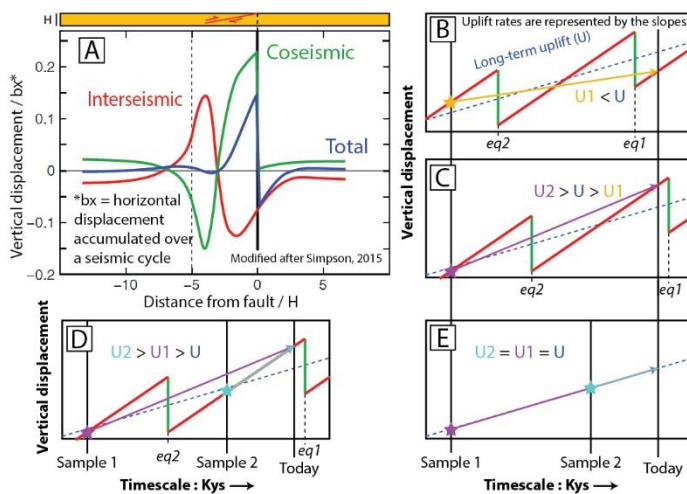
566 Rock uplift rates are of interest to try to understand the seismic behavior of the region.
 567 Short-term uplift rates, based on Holocene dates, have been observed to be very different from those
 568 obtained on longer time scales (usually from Pleistocene marine terraces) [92–94]. On a small time
 569 scale of a few thousand years, coseismic and interseismic vertical movements are a major component
 570 of the total vertical displacement [95]. Hence, in this context, the timing of sample deposition and
 571 current time position within the seismic cycle is expected to be an important factor influencing the
 572 short-term uplift rates (see Fig. 10).

573 Uplift calculations based on Holocene samples have been attempted by previous authors
 574 [48,29,10,5,28] and are also presented here based on our results (section 3.4, Table 3). Holocene mean
 575 uplift rates from near the middle of Beris beach are very high, varying between 2.9 and 3.75 mm/yr.
 576 These values fit quite well with the Late Pleistocene trends obtained from marine terraces [19],
 577 where long-term uplift rates along Beris beach increase from from 1 to 5 mm/yr going from west to
 578 east. Note that the uncertainties regarding the Pleistocene uplift trend along Beris beach are high due
 579 to local lack of data [19], which makes comparison to Holocene rates dubious. However, the fast
 580 Holocene uplift rates obtained here emphasize the highly active nature of tectonics in this region.

581 Table 4. Holocene uplift rates. Uplift rates based on lagoonal deposits are more precise due to their
 582 low IR, compared to beach deposits. More details in supplementary table S1.4.

Area	Sample	Deposits	Age $\pm 2\sigma$ [yr]	Mean Uplift rate since Age [mm/yr]	Pleistocene uplift rate [19] [mm/yr]
Chabahar bay	RN15-24	Beach	4010 \pm 135	1.29 \pm 0.9	~0.6
	RN16-18	Lagoon	7167 \pm 101	1.88 \pm 0.2	~0.6
	RN16-29	Lagoon	6138 \pm 117	1.38 \pm 0.4	~0.6
Beris beach	RN15-89	Beach	4506 \pm 131	2.92 \pm 1.2	1 to 4
	RN16-41	Lagoon	8432 \pm 88	3.38 \pm 0.2	1 to 4
	RN17-44 (OSL)	Beach	4576 \pm 454	3.75 \pm 1.8	1 to 4

583



584

585 Figure 10. Scenarios of vertical displacements on a seismically active subduction zone. eq:
 586 earthquake. (a) Vertical deformation distribution based on a viscoelastic model of elastic rebound for
 587 a thrust earthquake [90]. Our example scenarios of Fig. 10b to 10d are at \sim 5H from the trench
 588 (dashed black line), where coseismic subsidence and interseismic uplift occurs. (b) and (c) show two
 589 different scenarios, where sample deposition and current position occur at different moments within
 590 the seismic cycle. Red and green lines represent respectively the interseismic and coseismic
 591 movement of the continent (overriding plate of a subduction thrust). The short-term uplift calculated
 592 from the Holocene beach uplift (U_1 , U_2) can potentially be very variable, as well as different from the
 593 long-term uplift calculated (from emerged marine terraces) over a multitude of seismic cycles (U).
 594 Note that today's position in the seismic cycle seems to be an important factor determining
 595 calculated short term uplift rates: If a coseismic subsidence event recently happened, we can expect
 596 U_1 to be generally lower than U (Fig. 10b), and inversely (reversed behavior for coseismic uplift). Do
 597 fast Holocene rates calculated for the Makran imply an upcoming coseismic subsidence earthquake
 598 (like in Fig. 10c)? (d) Example showing how samples with different ages having different uplift rates

599 suggest a non-linear history of vertical displacements. (e) Example where continuous deformation
600 happens without coseismic vertical displacements, U_1 , U_2 and U are expected to be equal.

601 In Chabahar bay, previous uplift results vary substantially, ranging from 0.7 to 4.75 mm/yr
602 [28,29]. Our mean Holocene uplift rates in the western Chabahar bay vary between 1.3 and 1.9
603 mm/yr. Both ours and previous results are higher than the predicted long-term trend of ~ 0.6 mm/yr
604 obtained from the Konarak marine terraces situated 10 km southwards [19].

605 Holocene uplift rates obtained from lagoonal and beach deposits in Chabahar bay are much
606 higher than Pleistocene uplift rates obtained from marine terraces. Moreover, within the same beach,
607 calculated uplift rates differ, depending on the age of the considered sample (i.e., the time
608 considered for averaging the uplift rate) (Table 4) (see Fig. 10d). This indicates a complex history of
609 vertical movements on time scales of less than several millennia, possibly related to earthquakes. We
610 do not currently have sufficient data to provide a clear picture of the vertical motion of this region
611 over the Holocene. However, the fact that short-term and long-term uplift trends are different (e.g.,
612 Fig. 10b, 10c) might indicate that the Chabahar region is strongly influenced by large, infrequent
613 earthquakes.

614 6. Conclusion

615 In this study, we have presented sedimentological data along with dating to show the evolution
616 of the coastal Makran in Iran during the Holocene. Results from two studied beach sections indicate
617 that since 8400 BP, the coastal region of the Makran was occupied by the sea. Coastal lagoons were
618 progressively submerged with time until the maximum Holocene transgression. Since then,
619 deposition was dominated by prograding sequences of tidal and beach deposits. Variation in the
620 rate of coastal progradation during the Late Holocene seems to be strongly linked to the migration of
621 fluvial sedimentary input from one bay to another.

622 Our observations are in line with what might be expected on an uplifting coast. However, some
623 geomorphological and sedimentological singularities indicate the possible occurrence of at least one
624 megathrust earthquake events during the Holocene. In Chabahar bay, we observed a flooding
625 surface within the Late Holocene sedimentary succession, which we dated at 3150 years BP from two
626 (underlying and overlying) OSL results. We attribute this sudden relative sea-level rise to coseismic
627 subsidence. Additionally, short-term uplift rates obtained from our Holocene samples vary
628 depending on the timescale considered, which might indicate a complex history of vertical
629 displacements, possibly linked to earthquakes.

630 **Supplementary Materials:** The following are available online at www.mdpi.com/xxx/s1, Table S1: Published
631 Makran beach dating results, Pozm bay GPS data, Uplift rate calculation method and observed facies
632 descriptions. Data repository: [54], field pictures, radiocarbon dating analytical details, OSL dating analytical
633 details.

634 **Author Contributions:** Conceptualization, Raphaël Normand and Guy Simpson; Formal analysis, Raphaël
635 Normand, Frédéric Herman and Rabiul Haque Biswas; Funding acquisition, Guy Simpson; Investigation,
636 Raphaël Normand, Guy Simpson, Frédéric Herman, Rabiul Haque Biswas and Abbas Bahroudi; Methodology,
637 Raphaël Normand; Project administration, Guy Simpson and Abbas Bahroudi; Resources, Frédéric Herman and
638 Rabiul Haque Biswas; Visualization, Raphaël Normand; Writing – original draft, Raphaël Normand; Writing –
639 review & editing, Raphaël Normand, Guy Simpson, Frédéric Herman, Rabiul Haque Biswas and Abbas
640 Bahroudi.

641 **Funding:** This work was funded by the Swiss National Science Foundation, project n°200021_155904.

642 **Acknowledgments:** We are grateful to Reza Ensani, Feisal Arjomandi, Nurrudin Mazarzehi, Yousef Adeeb and
643 Gholamreza Hosseinyar for helping us with logistics in Iran and accompanying us in the field. We also would
644 like to thank the analytical assistance of Irka Hajdas for radiocarbon dating, Agathe Martignier for SEM,
645 Annette Süssenberger and Emanuelle Ricchi for XRD analysis.

646 **Conflicts of Interest:** The authors declare no conflict of interest.

647 **Appendix A**

648 If the method section is too long, we can try to arrange to put some of its content to the
649 Appendix (e.g., sections 3.3 and 3.4).

650 **References**

- 651 1. Falcon, N. L. Raised beaches and terraces of the Iranian Makran coast. *Geogr. J.* **1947**, *109*, 149–151
- 652 2. Snead, R. J. Recent Morphological changes along the coast of West Pakistan. *Ann. Assoc. Am. Geogr.* **1967**,
653 *57*, 550–565 doi:10.1111/j.1467-8306.1967.tb00621.x
- 654 3. Reyss, J. L., Pirazzoli, P. A., Haghypour, A., Hatté, C., & Fontugne, M. Quaternary marine terraces and
655 tectonic uplift rates on the south coast of Iran. *Geol. Soc. London, Spec. Publ.* **1998**, *146*, 225–237
656 doi:10.1144/GSL.SP.1999.146.01.13
- 657 4. Byrne, D. E., Sykes, L. R., & Davis, D. M. Great Thrust Earthquakes and Aseismic Slip Along the Plate
658 Boundary of the Makran Subduction Zone. *J. Geophys. Res. Earth* **1992**, *97*, 449–478 doi:10.1029/91JB02165
- 659 5. Page, W. D., Alt, J. N., Cluff, L. S., & Plafker, G. Evidence for the recurrence of large-magnitude earthquake
660 along the Makran coast of Iran and Pakistan. *Tectonophysics* **1979**, *52*, 533–547
661 doi:10.1016/0040-1951(79)90269-5
- 662 6. Ambraseys, N. N., & Melville, C. P. *A history of Persian earthquakes*. Cambridge University Press,
663 Cambridge, 1982, doi:10.1002/eqe.4290110412
- 664 7. Quittmeyer, R. C., & Jacob, K. H. Historical and Modern seismicity of Pakistan, Afghanistan,
665 Northwestern India, and Southeastern Iran. *Bull. Seismol. Soc. Am.* **1979**, *69*, 773–823
- 666 8. Heidarzadeh, M., Pirooz, M. D., Zaker, N. H., Yalciner, A. C., Mokhtari, M., & Esmaeily, A. Historical
667 tsunami in the Makran Subduction Zone off the southern coasts of Iran and Pakistan and results of
668 numerical modeling. *Ocean Eng.* **2008**, *35*, 774–786 doi:10.1016/j.oceaneng.2008.01.017
- 669 9. Musson, R. M. W. Subduction in the Western Makran: the historian's contribution. *J. Geol. Soc. London.*
670 **2009**, *166*, 387–391 doi:10.1144/0016-76492008-119
- 671 10. Rajendran, C. P., Rajendran, K., Shah-hosseini, M., Beni, A. N., Nautiyal, C. M., & Andrews, R. The hazard
672 potential of the western segment of the Makran subduction zone, northern Arabian Sea. *Nat. Hazards* **2013**,
673 *65*, 219–239 doi:10.1007/s11069-012-0355-6
- 674 11. Smith, G. L., McNeill, L. C., Wang, K., He, J., & Henstock, T. J. Thermal structure and megathrust
675 seismogenic potential of the Makran subduction zone. *Geophys. Res. Lett.* **2013**, *40*, 1528–1533
676 doi:10.1002/grl.50374
- 677 12. Penney, C., Tavakoli, F., Saadat, A., Nankali, H. R., Sedighi, M., Khorrami, F., Sobouti, F., Rafi, Z., Copley,
678 A., Jackson, J., & Priestley, K. Megathrust and accretionary wedge properties and behaviour in the Makran
679 subduction zone. *Geophys. J. Int.* **2017**, *209*, 1800–1830 doi:10.1093/gji/ggx126
- 680 13. Darwin, C. *Geological Observations on South America*. Cambridge University Press, Cambridge, 1846,
681 doi:10.1017/CBO9780511910180
- 682 14. Atwater, B. F., Musumi-Rokkaku, S., Satake, K., Tsuji, Y., Ueda, K., & Yamaguchi, D. K. *The Orphan*
683 *Tsunami of 1700—Japanese clues to a parent earthquake in North America*. University of Washington Press, U.S.
684 Geological Survey Professional Paper 1707, 2005, doi:10.3133/pp1707
- 685 15. McSaveney, M. J., Graham, I. J., Begg, J. G., Beu, A. G., Hull, A. G., Kim, K., & Zondervan, A. Late
686 Holocene uplift of beach ridges at Turakirae Head, south Wellington coast, New Zealand. *New Zeal. J. Geol.*
687 *Geophys.* **2006**, *49*, 337–358 doi:10.1080/00288306.2006.9515172
- 688 16. Monecke, K., Templeton, C. K., Finger, W., Houston, B., Luthi, S., Mcadoo, B. G., Meilianda, E., Storms, J.
689 E. A., Walstra, D., Amna, R., Hood, N., Karmanocky, F. J., Rusydy, I., & Unggul, S. Beach ridge patterns in
690 West Aceh, Indonesia, and their response to large earthquakes along the northern Sunda trench. *Quat.*
691 *Sci. Rev.* **2015**, *113*, 159–170 doi:10.1016/j.quascirev.2014.10.014
- 692 17. Vita-Finzi, C. Recent coastal deformation near the Strait of Hormuz. *Proc. R. Soc. Lond.* **1982**, *382*, 441–457
693 doi:10.1098/rspa.1982.0111
- 694 18. Snead, R. J. Uplifted Marine Terraces along the Makran coast of Pakistan and Iran. in *Himalaya to the Sea* ed.
695 Shroder, J. F. J. Routledge, London, 1993, 327–362
- 696 19. Normand, R., Simpson, G., Herman, F., Biswas, R. H., Bahroudi, A., & Schneider, B. Dating and
697 morpho-stratigraphy of uplifted marine terraces in the Makran subduction zone (Iran). *Earth Surf. Dyn.*
698 **2019**, *7*, 321–344 doi:10.5194/esurf-7-321-2019

- 699 20. Pararas-Carayannis, G. The Potential of Tsunami Generation along the Makran Subduction. *Sci. Tsunami*
700 *hazards* **2006**, *24*, 358–384
- 701 21. Hafeez, H. The potential of tsunami generation along Karachi and the Makran coast of Pakistan. *Pakistan J.*
702 *Meteorol.* **2007**, *4*, 25–40 doi:10.1007/s10661-018-7048-x
- 703 22. Rajendran, C. P., Ramanamurthy, M. V., Reddy, N. T., & Rajendran, K. Hazard implications of the late
704 arrival of the 1945 Makran tsunami. *Curr. Sci.* **2008**, *95*, 1739–1743
- 705 23. Heidarzadeh, M., & Kijko, A. A probabilistic tsunami hazard assessment for the Makran subduction zone
706 at the northwestern Indian Ocean. *Nat. Hazards* **2011**, *56*, 577–593 doi:10.1007/s11069-010-9574-x
- 707 24. Schneider, B., Hoffmann, G., & Reicherter, K. Scenario-based tsunami risk assessment using a static
708 flooding approach and high-resolution digital elevation data: An example from Muscat in Oman. *Glob.*
709 *Planet. Change* **2016**, *139*, 183–194 doi:10.1016/j.gloplacha.2016.02.005
- 710 25. Hoffmann, G., Reicherter, K., Wiatr, T., Grützner, C., & Rausch, T. Block and boulder accumulations along
711 the coastline between Fins and Sur (Sultanate of Oman): tsunamigenic remains? *Nat. Hazards* **2013**, *65*,
712 851–873 doi:10.1007/s11069-012-0399-7
- 713 26. Donato, S. V., Reinhardt, E. G., Boyce, J. I., Pilarczyk, J. E., & Jupp, B. P. Particle-size distribution of
714 inferred tsunami deposits in Sur Lagoon, Sultanate of Oman. *Mar. Geol.* **2009**, *257*, 54–64
715 doi:10.1016/j.margeo.2008.10.012
- 716 27. Shah-Hosseini, M., Morhange, C., Naderi Beni, A., Marriner, N., Lahijani, H., Hamzeh, M., & Sabatier, F.
717 Coastal boulders as evidence for high-energy waves on the Iranian coast of Makran. *Mar. Geol.* **2011**, *290*,
718 17–28 doi:10.1016/j.margeo.2011.10.003
- 719 28. Shah-Hosseini, M., Ghanavati, E., Morhange, C., Naderi Beni, A., Lahijani, H. A., & Hamzeh, M. A. The
720 evolution of Chabahar beach ridge system in SE Iran in response to Holocene relative sea level changes.
721 *Geomorphology* **2018**, *318*, 139–147 doi:10.1016/j.geomorph.2018.06.009
- 722 29. Gharibreza, M. Evolutionary trend of paleoshorelines in the Coastal Makran zone (Southeast Iran) since
723 the mid-Holocene. *Quat. Int.* **2016**, *392*, 203–212 doi:10.1016/j.quaint.2015.06.030
- 724 30. Gharibreza, M. R., & Motamed, A. Late Quaternary Paleoshorelines and Sedimentary Sequences in
725 Chabahar Bay (Southeast of Iran). *J. Coast. Res.* **2006**, *226*, 1499–1504 doi:10.2112/05A-0020.1
- 726 31. Zare, M., Amini, H., Yazdi, P., Sesetyan, K., Demircioglu, M. B., Kalafat, D., Erdik, M., Giardini, D., Khan,
727 M. A., & Tsereteli, N. Recent developments of the Middle East catalog. *J. Seismol.* **2014**, *18*, 749–772
728 doi:10.1007/s10950-014-9444-1
- 729 32. Smith, G., McNeill, L., Henstock, I. J., & Bull, J. The structure and fault activity of the Makran accretionary
730 prism. *J. Geophys. Res. Solid Earth* **2012**, *117*, 1–17 doi:10.1029/2012JB009312
- 731 33. Vernant, P., Nilforoushan, F., Hatzfeld, D., Abbassi, M. R., Vigny, C., Masson, F., Nankali, H., Martinod, J.,
732 Ashtiani, A., Bayer, R., Tavakoli, F., & Chéry, J. Present-day crustal deformation and plate kinematics in
733 the Middle East constrained by GPS measurements in Iran and northern Oman. *Geophys. J. Int.* **2004**, *157*,
734 381–398 doi:10.1111/j.1365-246X.2004.02222.x
- 735 34. Masson, F., Anvari, M., Djamour, Y., Walpersdorf, A., Tavakoli, F., Daignières, M., Nankali, H., & Van
736 Gorp, S. Large-scale velocity field and strain tensor in Iran inferred from GPS measurements: New insight
737 for the present-day deformation pattern within NE Iran. *Geophys. J. Int.* **2007**, *170*, 436–440
738 doi:10.1111/j.1365-246X.2007.03477.x
- 739 35. Khan, M. A., Bendick, R., Bhat, M. I., Bilham, R., Kakar, D. M., Khan, S. F., Lodi, S. H., Qazi, M. S., Singh,
740 B., Szeliga, W., & Wahab, A. Preliminary geodetic constraints on plate boundary deformation on the
741 western edge of the Indian plate from TriGGnet (Tri-University GPS Geodesy Network). *J. Himal. Earth*
742 *Sci.* **2008**, *41*, 71–87
- 743 36. Vita-Finzi, C. Neotectonics in the Arabian Sea coasts. *Geol. Soc. London, Spec. Publ.* **2002**, *195*, 87–96
744 doi:10.1144/GSL.SP.2002.195.01.06
- 745 37. Burg, J.-P., Dolati, A., Bernoulli, D., & Smit, J. Structural style of the Makran Tertiary accretionary complex
746 in SE-Iran. in *Lithosphere Dynamics and Sedimentary Basins: The Arabian Plate and Analogues* eds. Al Hosani,
747 K., Roure, F., Ellison, R. & Lokier, S. Springer, 2012, 239–259 doi:10.1007/978-3-642-30609-9_12
- 748 38. McCall, G. J. H. A summary of the geology of the Iranian Makran. *Geol. Soc. London, Spec. Publ.* **2002**, *195*,
749 147–204 doi:10.1144/GSL.SP.2002.195.01.10
- 750 39. Harrison, J. V. Coastal Makran : Discussion. *Geogr. J.* **1941**, *97*, 1–15
- 751 40. Harms, J. C., Cappel, H. N., & Francis, D. C. The Makran Coast of Pakistan: It's Stratigraphy and
752 Hydrocarbon Potential. in *Marine Geology and Oceanography of Arabian Sea and Coastal Pakistanography of*

- 753 *Arabian Sea and Coastal Pakistan* eds. Haq, B. U. & Milliman, J. D. Van Nostrand Reinhold Company Inc.,
754 1984, 3–26
- 755 41. Ghorashi, M. Late Cainozoic faulting in S.E. Iran. PhD Thesis, University College London, 1978,
756 42. Blanford, W. T. Note on the geological formations seen along the coasts of Bilúchistán and Persia from
757 Karáchí to the head of the Persian Gulf, and on some of the Gulf Islands. *Rec. Geol. Surv. India* **1872**, *5*, 41–45
758
- 759 43. Stiffe, A. W. On the Mud-craters and Geological Structure of the Mekran Coast. *Q. J. Geol. Soc. London* **1874**,
760 *30*, 50–53 doi:10.1144/GSL.JGS.1874.030.01-04.24
- 761 44. Ivory, S. J., & Lézine, A. M. Climate and environmental change at the end of the Holocene Humid Period:
762 A pollen record off Pakistan. *Comptes Rendus - Geosci.* **2009**, *341*, 760–769 doi:10.1016/j.crte.2008.12.009
- 763 45. Prins, M. A., Postma, G., Cleveringa, J., Cramp, A., & Kenyon, N. H. Controls on terrigenous sediment
764 supply to the Arabian Sea during the late quaternary: The Indus fan. *Mar. Geol.* **2000**, *169*, 327–349
765 doi:10.1016/S0025-3227(00)00086-4
- 766 46. Bourget, J., Zaragosi, S., Ellouz-Zimmermann, S., Ducassou, E., Prins, M. A., Garlan, T., Lanfume, V.,
767 Schneider, J. L., Rouillard, P., & Giraudeau, J. Highstand vs. lowstand turbidite system growth in the
768 Makran active margin: Imprints of high-frequency external controls on sediment delivery mechanisms to
769 deep water systems. *Mar. Geol.* **2010**, *274*, 187–208 doi:10.1016/j.margeo.2010.04.005
- 770 47. Sanlaville, P., Besenval, R., Evin, J., & Prieur, A. Evolution de la région littorale du Makran pakistanais à
771 l'Holocène. *Paléorient* **1991**, *17*, 3–18 doi:10.3406/paleo.1991.4536
- 772 48. Haghypour, N., Burg, J. P., Ivy-Ochs, S., Hajdas, I., Kubik, P., & Christl, M. Correlation of fluvial terraces
773 and temporal steady-state incision on the onshore Makran accretionary wedge in southeastern Iran:
774 Insight from channel profiles and ¹⁰Be exposure dating of strath terraces. *Bull. Geol. Soc. Am.* **2014**, *127*,
775 560–583 doi:10.1130/B31048.1
- 776 49. Little, R. D. Terraces of the Makran Coast of Iran and parts of West Pakistan. PhD Thesis, University of
777 Southern California, 1972,
- 778 50. Saket, A., & Etemad-shahidi, A. Wave energy potential along the northern coasts of the Gulf of Oman ,
779 Iran. *Renew. Energy* **2012**, *40*, 90–97 doi:10.1016/j.renene.2011.09.024
- 780 51. Saket, A., Etemad-shahidi, A., & Moeini, M. H. Evaluation of ECMWF wind data for wave hindcast in
781 Chabahar zone. *J. Coast. Res.* **2013**, 380–385 doi:10.2112/SI65-065.1
- 782 52. Vita-Finzi, C. ¹⁴C Dating of recent crustal movements in the Persian Gulf and Iranian Makran. *Radiocarbon*
783 **1980**, *22*, 763–773 doi:10.1017/S0033822200010134
- 784 53. Sanlaville, P., & Dalongeville, R. L'évolution des espaces littoraux du golfe Persique et du golfe d'Oman
785 depuis la phase finale de la transgression post-glaciaire. *Paléorient* **2018**, *31*, 9–26
786 doi:10.3406/paleo.2005.4780
- 787 54. Normand, R., Simpson, G., Herman, F., Biswas, R. H., & Bahroudi, A. Data for: Holocene coastal evolution
788 of the eastern Iranian Makran: Insights on seismic activity based on beach morphology and
789 sedimentology. **2019**, doi:10.5281/zenodo.2558320
- 790 55. Hajdas, I. Radiocarbon dating and its applications in Quaternary studies. *Quat. Sci. J. - Eiszeitalter und*
791 *Gegenwart* **2008**, *57*, 2–24 doi:10.3285/eg.57.1-2.1
- 792 56. Bronk Ramsey, C., & Lee, S. Recent and Planned Developments of the Program OxCal. *Radiocarbon* **2013**,
793 *55*, 720–730 doi:10.2458/azu_js_rc.55.16215
- 794 57. Reimer, P. *et al.* IntCal13 and Marine13 Radiocarbon Age Calibration Curves 0–50,000 Years cal BP.
795 *Radiocarbon* **2013**, *55*, 1869–1887 doi:10.2458/azu_js_rc.55.16947
- 796 58. Southon, J., Kashgarian, M., Fontugne, M., Metivier, B., & Yim, W. W.-S. Marine reservoir correction for
797 the Indian Ocean and Southeast Asia. *Radiocarbon* **2002**, *44*, 167–180 doi:10.1017/S0033822200064778
- 798 59. von Rad, U., Schaaf, M., Michels, K. H., Schulz, H., Berger, W. H., & Sirocko, F. A 5000-yr Record of
799 Climate Change in Varved Sediments from the Oxygen Minimum Zone off Pakistan, Northeastern
800 Arabian Sea. *Quat. Res.* **1999**, *51*, 39–53 doi:10.1006/qres.1998.2016
- 801 60. Murray, A. S., & Olley, J. M. Precision and accuracy in the optically stimulated luminescence dating of
802 sedimentary quartz: A status review. *Geochronometria* **2002**, *21*, 1–16
- 803 61. Lamothe, M. Luminescence dating of interglacial coastal depositional systems: Recent developments and
804 future avenues of research. *Quat. Sci. Rev.* **2016**, *146*, 1–27 doi:10.1016/j.quascirev.2016.05.005
- 805 62. Murray, A. S., & Wintle, A. G. Luminescence dating of quartz using an improved single-aliquot
806 regenerative-dose protocol. *Radiat. Meas.* **2000**, *32*, 57–73 doi:10.1016/S1350-4487(99)00253-X

- 807 63. Duller, G. A. T. The Analyst software package for luminescence data : overview and recent improvements.
808 *Anc. TL* **2015**, *33*, 35–42
- 809 64. Galbraith, R. F., Roberts, R. G., Laslett, G. M., Yoshida, H., & Olley, J. M. Optical dating of single and
810 multiple grains of quartz from Jinmium rock shelter, Northern Australia: Part I, Experimental design and
811 statistical models. *Archaeometry* **1999**, *41*, 339–364 doi:10.1111/j.1475-4754.1999.tb00987.x
- 812 65. Durcan, J. A., King, G. E., & Duller, G. A. T. DRAC : Dose Rate and Age Calculator for trapped charge
813 dating. *Quat. Geochronol.* **2015**, *28*, 54–61 doi:10.1016/j.quageo.2015.03.012
- 814 66. Murray, A. S., & Wintle, A. G. The single aliquot regenerative dose protocol: Potential for improvements in
815 reliability. *Radiat. Meas.* **2003**, *37*, 377–381 doi:10.1016/S1350-4487(03)00053-2
- 816 67. Pirazzoli, P. A. *World atlas of Holocene Sea-level changes*. Elsevier B.V., 1991,
- 817 68. Lambeck, K. Shoreline reconstructions for the Persian Gulf since the last glacial maximum. *Earth Planet.*
818 *Sci. Lett.* **1996**, *142*, 43–57 doi:10.1016/0012-821X(96)00069-6
- 819 69. Hibbert, F. D., Williams, F. H., Fallon, S. J., & Rohling, E. J. A database of biological and geomorphological
820 sea-level markers from the Last Glacial Maximum to present. *Sci. Data* **2018**, *5*, 1–25
821 doi:10.1038/sdata.2018.88
- 822 70. Rovere, A., Raymo, M. E., Vacchi, M., Lorscheid, T., Stocchi, P., Gómez-Pujol, L., Harris, D. L., Casella, E.,
823 O’Leary, M. J., & Hearty, P. J. The analysis of Last Interglacial (MIS 5e) relative sea-level indicators:
824 Reconstructing sea-level in a warmer world. *Earth-Science Rev.* **2016**, *159*, 404–427
825 doi:10.1016/j.earscirev.2016.06.006
- 826 71. Lajoie, K. R. Coastal Tectonics. in *Active Tectonics: Impact on Society* ed. Wallace, R. Washington DC:
827 National Academy Press, 1986, 95–124
- 828 72. Otvos, E. G. Beach ridges — definitions and significance. *Geomorphology* **2000**, *32*, 83–108
829 doi:10.1016/S0169-555X(99)00075-6
- 830 73. Tamura, T. Beach ridges and prograded beach deposits as palaeoenvironment records. *Earth-Science Rev.*
831 **2012**, *114*, 279–297 doi:10.1016/j.earscirev.2012.06.004
- 832 74. Pedoja, K., Husson, L., Bezou, A., Pastier, A., Imran, A. M., Arias-Ruiz, C., Sarr, A., Elliot, M.,
833 Pons-Branchu, E., Nexer, M., Regard, V., Hafidz, A., Robert, X., Benoit, L., Delcaillau, B., Authemayou, C.,
834 Dumoulin, C., & Choblet, G. On the long-lasting sequences of coral reef terraces from SE Sulawesi
835 (Indonesia): Distribution, formation, and global significance. *Quat. Sci. Rev.* **2018**, *188*, 37–57
836 doi:10.1016/j.quascirev.2018.03.033
- 837 75. Bird, E. *Coastal Geomorphology, an introduction*. Wiley, 2000,
- 838 76. Ashton, A., Murray, A. B., & Arnault, O. Formation of coastline features by large-scale instabilities
839 induced by high-angle waves. *Nature* **2001**, *414*, 296–300 doi:10.1038/35104541
- 840 77. Valvo, L. M., Murray, A. B., & Ashton, A. How does underlying geology affect coastline change? An
841 initial modeling investigation. *J. Geophys. Res.* **2006**, *111*, doi:10.1029/2005JF000340
- 842 78. Limber, P. W., Murray, A. B., Adams, P. N., & Goldstein, E. B. Unraveling the dynamics that scale
843 cross-shore headland relief on rocky coastlines: 1. Model development. *J. Geophys. Res. Earth Surf.* **2014**,
844 *119*, 854–873 doi:10.1002/2013JF002950
- 845 79. Schwanghart, W., & Kuhn, N. J. TopoToolbox : A set of Matlab functions for topographic analysis. *Environ.*
846 *Model. Softw.* **2010**, *25*, 770–781 doi:10.1016/j.envsoft.2009.12.002
- 847 80. Schwanghart, W., & Scherler, D. Short Communication : TopoToolbox 2 – MATLAB-based software for
848 topographic analysis and modeling in Earth surface sciences. *Earth Surf. Dyn.* **2014**, *2*, 1–7
849 doi:10.5194/esurf-2-1-2014
- 850 81. Limber, P. W., & Murray, A. B. Unraveling the dynamics that scale cross-shore headland relief on rocky
851 coastlines: 2. Model predictions and initial tests. *J. Geophys. Res. Earth Surf.* **2014**, *119*, 874–891
852 doi:10.1002/2013JF002978
- 853 82. Hurst, M. D., Barkwith, A., Ellis, M. A., Thomas, C. W., & Murray, A. B. Exploring the sensitivities of
854 crenulate bay shorelines to wave climates using a new vector-based one-line model. *J. Geophys. Res. Earth*
855 *Surf.* **2015**, 2586–2608 doi:10.1002/2015JF003704
- 856 83. Yasso, W. E. Plan Geometry of Headland-Bay Beaches. *J. Geol.* **1965**, *73*, 702–714 doi:10.1086/627111
- 857 84. Axe, P., Ilic, S., & Chadwick, A. Evaluation of beach modelling techniques behind detached breakwaters.
858 in *Coastal Engineering Proceedings* 1996, *25*, 2036–2049 doi:10.1061/9780784402429.158
- 859 85. Schneider, B. Tsunami and storm sediments in Oman : Characterizing extreme wave deposits using
860 terrestrial laser scanning. *J. Coast. Conserv.* **2018**, doi:10.1007/s11852-018-0663-4

- 861 86. Plafker, G. Tectonics of the March 27, 1964 Alaska Earthquake. in *The Alaska Earthquake, March 27, 1964,*
862 *Regional Effects* U.S. Government Printing Office, 1966, 74 doi:10.3133/pp543
- 863 87. Plafker, G., & Savage, J. C. Mechanism of the Chilean Earthquakes of May 21 and 22, 1960. *Geol. Soc. Am.*
864 *Bull.* **1970**, *81*, 1001–1030 doi:10.1130/0016-7606(1970)81[1001:MOTCEO]2.0.CO;2
- 865 88. Sato, T., & Matsu'ura, M. Cyclic crustal movement, steady uplift of marine terraces, and evolution of the
866 island arc-trench system in southwest Japan. *Geophys. J. Int.* **1992**, *111*, 617–629
867 doi:10.1111/j.1365-246X.1992.tb02116.x
- 868 89. Fariás, M., Vargas, G., Tassara, A., Carretier, S., Baize, S., Melnick, D., & Bataille, K. Land-Level Changes
869 Produced by the Mw 8.8 2010 Chilean Earthquake. *Science (80-.)*. **2010**, *329*, 916
870 doi:10.1126/science.1192094
- 871 90. Simpson, G. Accumulation of permanent deformation during earthquake cycles on reverse faults. *J.*
872 *Geophys. Res. Solid Earth* **2015**, *120*, 1958–1974 doi:10.1002/2014JB011442
- 873 91. Savage, J. C. A Dislocation Model of Strain Accumulation and Release at a Subduction Zone. *J. Geophys.*
874 *Res.* **1983**, *88*, 4984–4996 doi:10.1029/JB088iB06p04984
- 875 92. Ota, Y., & Yamaguchi, M. Holocene coastal uplift in the western Pacific Rim in the context of late
876 Quaternary uplift. *Quat. Int.* **2004**, *120*, 105–117 doi:10.1016/j.quaint.2004.01.010
- 877 93. Pedoja, K., Husson, L., Johnson, M. E., Melnick, D., Witt, C., Pochat, S., Nexer, M., Delcaillau, B., Pinegina,
878 T., Poprawski, Y., Authemayou, C., Elliot, M., Regard, V., & Garestier, F. Coastal staircase sequences
879 reflecting sea-level oscillations and tectonic uplift during the Quaternary and Neogene. *Earth-Science Rev.*
880 **2014**, *132*, 13–38 doi:10.1016/j.earscirev.2014.01.007
- 881 94. Pinegina, T. K., Bourgeois, J., Kravchunovskaya, E. A., Lander, A. V., Arcos, M. E. M., Pedoja, K., &
882 MacInnes, B. T. A nexus of plate interaction: Vertical deformation of holocene wave-built terraces on the
883 kamchatsky peninsula (kamchatka, russia). *Bull. Geol. Soc. Am.* **2013**, *125*, 1554–1568 doi:10.1130/B30793.1
- 884 95. Wesson, R. L., Melnick, D., Cisternas, M., Moreno, M., & Ely, L. L. Vertical deformation through a
885 complete seismic cycle at Isla Santa María , Chile. *Nat. Geosci.* **2015**, *8*, 547–553 doi:10.1038/NGEO2468
- 886 96.



© 2019 by the authors. Submitted for possible open access publication under the terms and conditions of the Creative Commons Attribution (CC BY) license (<http://creativecommons.org/licenses/by/4.0/>).